



Inelastic Response of High-Rise Buildings under Strong Winds: Accuracy of Reduced-Order Building Model and Influence of Biaxial Response Interaction

Jinghui Huang, S.M.ASCE¹; and Xinzhong Chen, M.ASCE²

Abstract: This study examined the accuracy of a reduced-order building model approach for inelastic response analysis of tall buildings under simultaneous actions of both alongwind and crosswind loadings. The reduced-order model was established following the modal push-over analysis procedure. The inelastic building response was represented by fundamental modes in principal directions. The hysteretic relationships of generalized restoring forces and displacements were determined by static modal pushover analysis using nonlinear finite element model with distributed plasticity. These relations were then represented by a biaxial hysteresis model, which leads to state-space equations of the building motion with a reduced-order building model that can be solved by response history analysis or by statistical linearization approach. A comprehensive analysis of response statistics of a 60-story building, including time-varying mean, standard deviation, kurtosis, and peak factors at different wind speeds was carried out using the reduced-order building model and computationally more demanding finite element model. The results demonstrate the accuracy of the reduced-order building model. The statistical linearization approach based on Gaussian response assumption can also offer quite accurate estimations, although it can be further improved by considering the non-Gaussian probability distribution of response caused by yielding. The interaction of inelastic alongwind and crosswind responses was addressed. The challenges faced in the estimation of time-varying mean component of inelastic response were also highlighted. **DOI: 10.1061/JSENDH/STENG-11069.** © 2022 American Society of Civil Engineers.

Author keywords: High-rise buildings; Inelastic response; Nonlinear finite element model; Modal pushover analysis; Hysteretic models; Statistical linearization; Alongwind response; Crosswind response; Biaxial interaction.

Introduction

Current building design to wind does not explicitly permit inelastic behavior even under ultimate wind loadings. This linear design approach may limit the use of more innovative tall building systems with improved performance and economy. The ASCE has recently published prestandard for performance-based wind design (PBWD) of buildings (ASCE 2019), which explicitly permits nonlinear dynamic analysis allowing limited inelasticity in the Main Wind Force Resisting System (MWFRS) elements. Currently, there is very little information in the literature concerning inelastic response of buildings to wind. Therefore, the actual capacity of buildings against extreme wind beyond linear elastic limit is unclear.

Hong (2004) and Gani and Légeron (2012) investigated the alongwind response of bilinear single-degree-of-freedom (SDOF) structures, discussed the relationship between the structural natural frequency and strength reduction factor for a given ductility factor, and confirmed that flexible structures can benefit more from ductility effect than rigid structures. Irwin (2009) discussed the

Note. This manuscript was submitted on November 1, 2021; approved on July 29, 2022; published online on October 21, 2022. Discussion period open until March 21, 2023; separate discussions must be submitted for individual papers. This paper is part of the *Journal of Structural Engineering*, © ASCE, ISSN 0733-9445.

potential benefits from an inelastic design procedure for wind-excited tall buildings. Judd and Charney (2015) implemented incremental dynamic analysis to study the inelastic behavior and collapse risk of SDOF buildings under uncoupled alongwind and crosswind excitations. Mooneghi et al. (2015) discussed construction of a tall building model in wind tunnel with bilinear restoring force character.

Inelastic response analysis of wind-excited tall buildings using nonlinear finite element (FE) building models can shed more insight on building performance. Tamura et al. (2001) studied the inelastic crosswind responses of 2D multistory building frames, and found that a column fracture immediately introduces a structural collapse mechanism. Griffis et al. (2013) proposed a performance-based wind engineering framework with an explicit consideration of nonlinear behavior. Beck et al. (2014) investigated the optimal stiffness of a hysteretic multiple-degree-of-freedom (MDOF) 2D reinforced concrete (RC) building frame subjected to zero-mean alongwind excitation. Hart and Jain (2014) presented performance-based wind evaluation and strengthening of existing concrete buildings, including performing a nonlinear dynamic analysis.

Judd and Charney (2016) presented nonlinear analysis of a 10-story steel building with OpenSees (Mckenna et al. 2010) under wind loads with different durations. Tabbuso et al. (2016) proposed a method for evaluating elastoplastic reliability of uncertain wind-excited structures using subset Monte Carlo simulation of alongwind response. Chuang and Spence (2017, 2019) investigated collapse probability of tall buildings based on dynamic shakedown theory. Mohammadi et al. (2019) conducted 3D response analysis of a 47-story steel high-rise building with incremental dynamic analysis approach. The results revealed robust lateral compacity in the overall lateral-load-resisting system, but also confirmed the

¹Ph.D. Candidate, National Wind Institute, Dept. of Civil, Environmental and Construction Engineering, Texas Tech Univ., Lubbock, TX 79409-1023. ORCID: https://orcid.org/0000-0003-0494-8299. Email: jinghui.huang@ttu.edu

²President's Excellence in Research Professor, National Wind Institute, Dept. of Civil, Environmental and Construction Engineering, Texas Tech Univ., Lubbock, TX 79409-1023 (corresponding author). Email: xinzhong .chen@ttu.edu

existence of unacceptable serviceability performance under various levels of wind loading in terms of large story drifts and floor accelerations. Ghaffary and Moustafa (2021) studied inelastic response of a 20-story steel moment-resisting frame through collapse under alongwind and crosswind loads acting separately using nonlinear OpenSees model. They confirmed that current code methods can result in overly conservative structural design and that permitting well-controlled inelastic response can help to achieve safer and more economical design. Ouyang and Spence (2021) presented a probabilistic assessment of structural and envelope damage of a 45-story steel building under alongwind loading through nonlinear dynamic analysis using a nonlinear FE model. Huang and Chen (2022) conducted a comprehensive analysis of the inelastic response of tall buildings under simultaneous actions of both alongwind and crosswind loads based on a 3D nonlinear FE model of a 60-story building. The second-order P-Delta effect on both elastic and inelastic responses was also examined.

Several studies have focused on simplified and computationally more effective estimations of uncoupled alongwind and crosswind inelastic building responses. Ohkuma et al. (1997) proposed an approach based on elastoplastic total energy input and energy response, showing that the peak inelastic displacement can be estimated with an error of less than 20%. Tsujita et al. (1997) introduced an approach based on the peak response distribution characteristics. Feng and Chen (2018) presented a comprehensive study on both alongwind and crosswind responses by considering the fundamental mode with bilinear restoring force character through response history analysis (RHA) and statistical linearization approach. The hysteretic relation between the generalized restoring force and displacement can be determined by static modal pushover analysis (MPA) using a nonlinear FE building model.

This study examined the accuracy of the MPA procedure for inelastic response analysis of tall buildings under simultaneous actions of both alongwind and crosswind loadings. The MPA procedure has been widely utilized to predict seismic demand of MDOF nonlinear buildings under single input of ground motion (e.g., Chopra and Goel 2002, 2004; Chopra et al. 2004; Goel and Chopra 2005; Kalkan and Kunnath 2007). The inelastic building response is represented by fundamental modes, similar to linear elastic response. The hysteretic relationships of generalized restoring forces and displacements are determined by static MPA using nonlinear FE building model under loads in both alongwind and crosswind directions. These relations are then represented by a biaxial hysteretic model (Park et al. 1986; Wang and Wen 2000; Harvey and Gavin 2014). The response statistics of a 60-story building under different wind speeds, including time-varying mean, standard deviation (STD), kurtosis, and peak factors, were quantified from RHA by solving the state-space equation. The response statistics were also calculated from an equivalent linear system via statistical linearization approach under Gaussian response assumption. A comprehensive parametric study covering a wide range of parameters, influencing inelastic responses under both uniaxial and biaxial wind loads, was carried out to examine the accuracy of the reduced building model developed from MPA procedure, and to examine the influence of the biaxial response interaction.

Analytical Framework

Equations of Motion of a Reduced-Order Building Model

The development of reduced-order building model based on MPA procedure is presented. The responses of a MDOF tall building in

two translational directions under wind excitations are considered. A nonlinear FE building model can be constructed. The governing equations of motion in terms of building story displacements are given by

$$M\ddot{u}_x + C_x\dot{u}_x + F_x(u_x, \dot{u}_x, u_y, \dot{u}_y) = P_x(t)$$
 (1a)

$$M\ddot{u}_y + C_y\dot{u}_y + F_y(u_x, \dot{u}_x, u_y, \dot{u}_y) = P_y(t)$$
 (1b)

where $u_x(t)$ and $u_y(t)$ = displacement vectors in two translational x and y directions; M = building mass matrix; C_x and C_y = damping matrices in both directions; $F_x(u_x,\dot{u}_x,u_y,\dot{u}_y)$ and $F_y(u_x,\dot{u}_x,u_y,\dot{u}_y)$ = nonlinear hysteretic restoring force vectors, which depend on displacements and velocities in both directions; $P_x(t)$ and $P_y(t)$ = dynamic wind load (including the mean components) vectors; t = time variable; and the overdot symbol denotes the derivative with time. When building response is within linear elastic range, we have $F_x(u_x,\dot{u}_x,u_y,\dot{u}_y) = K_xu_x$ and $F_y(u_x,\dot{u}_x,u_y,\dot{u}_y) = K_yu_y$, where K_x and K_y are stiffness matrices in both translational directions. It is assumed here that the linear elastic building responses in two translational directions are uncoupled.

It is assumed that the building response over the building height can be represented in terms of fundamental modes, as follows:

$$u_x(t) \approx \phi_x q_x(t); \qquad u_y(t) \approx \phi_y q_y(t)$$
 (2)

where $q_x(t)$ and $q_y(t)$ = modal (generalized) displacements (coordinates); and ϕ_x and ϕ_y = fundamental mode shapes in x and y directions of the corresponding linear system and are determined by following modal analysis:

$$\omega_x^2 M \phi_x = K_x \phi_x; \qquad \omega_y^2 M \phi_y = K_y \phi_y \tag{3}$$

where $\omega_x=2\pi f_x$ and $\omega_y=2\pi f_y$ are the fundamental mode frequencies of the corresponding linear system.

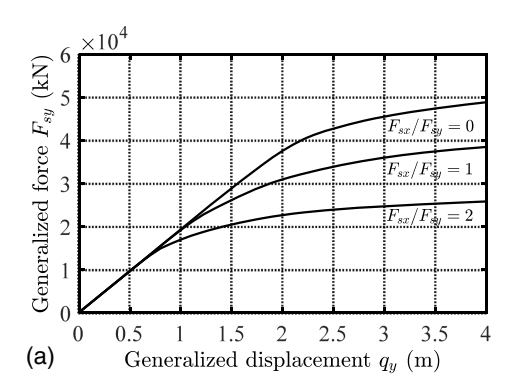
Substituting Eq. (2) into Eqs. (1a) and (1b) and premultiplying $\phi_x^{\rm T}$ and $\phi_y^{\rm T}$, respectively, leads to the following governing equations of the modal displacements:

$$M_x \ddot{q}_x + 2M_x \zeta_x \omega_x \dot{q}_x + F_{xx}(q_x, \dot{q}_x, q_y, \dot{q}_y) = Q_x \qquad (4a)$$

$$M_{\mathbf{v}}\ddot{q}_{\mathbf{v}} + 2M_{\mathbf{v}}\zeta_{\mathbf{v}}\omega_{\mathbf{v}}\dot{q}_{\mathbf{v}} + F_{s\mathbf{v}}(q_{\mathbf{x}},\dot{q}_{\mathbf{x}},q_{\mathbf{v}},\dot{q}_{\mathbf{v}}) = Q_{\mathbf{v}} \tag{4b}$$

where $M_x = \phi_x^T M \phi_x$ and $M_y = \phi_y^T M \phi_y$ are generalized mass; $\zeta_x = \phi_x^T C_x \phi_x / (2M_x \omega_x)$ and $\zeta_y = \phi_y^T C_y \phi_y / (2M_y \omega_y)$ are modal damping ratios; $F_{sx}(q_x, \dot{q}_x, q_y, \dot{q}_y) = \phi_x^T F_x (u_x, \dot{u}_x, u_y, \dot{u}_y)$ and $F_{sy}(q_x, \dot{q}_x, q_y, \dot{q}_y) = \phi_y^T F_y (u_x, \dot{u}_x, u_y, \dot{u}_y)$ are generalized nonlinear hysteretic restoring forces; and $Q_x(t) = \phi_x^T P_x(t)$ and $Q_y(t) = \phi_y^T P_y(t)$ are generalized forces. When building response is within linear elastic range, $F_{sx}(q_x, \dot{q}_x, q_y, \dot{q}_y) = K_x q_x = M_x \omega_x^2 q_x$ and $F_{sy}(q_x, \dot{q}_x, q_y, \dot{q}_y) = K_y q_y = M_y \omega_y^2 q_y$, and thus the equations of linear modal responses are uncoupled. When a building behaves beyond linear elastic range, the equations of motion become coupled, as the relationship between the restoring force and displacement in one direction is also affected by the response in another direction

The hysteretic relationships between the generalized restoring forces and displacements can be quantified via static MPA procedure through a static analysis using the nonlinear FE building model. The modal inertial forces in two directions are applied to the building model simultaneously which are given as $L_x = \alpha \omega_x^2 M \phi_x$ and $L_y = \beta \omega_y^2 M \phi_y$, where α and β are constants to control the magnitude of L_x and L_y . The static loads are monotonically increased with the invariant heightwise distributions, and the



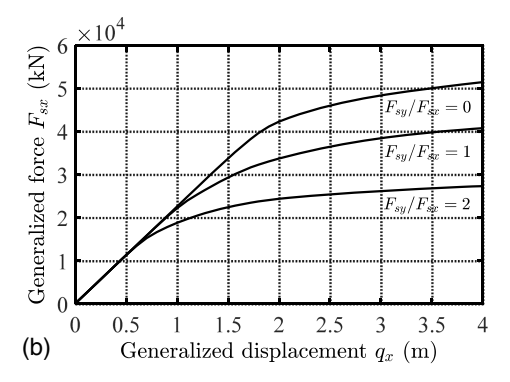


Fig. 1. Generalized force and deformation relations from the FE model: (a) alongwind (y); and (b) crosswind (x).

corresponding generalized displacements are calculated. The corresponding generalized restoring forces are $F_{sx} = \phi_x^T L_x$ and $F_{sy} = \phi_y^T L_y$. The generalized restoring force and generalized displacement relations are functions of F_{sx}/F_{sy} .

Fig. 1 shows such relationships of a tall building, which will be discussed in more detail in this work. It is evident that in the linear elastic range, the generalized restoring force and displacement in each direction follow a linear relationship whose slope is the generalized stiffness K_x or K_y . When yielding is developed and building shows nonlinear inelastic response, the hysteretic relation between the generalized force and displacement in one direction is also affected by the loading in another direction. A biaxial hysteretic model is required to model the relations of the generalized restoring forces and displacements.

Based on the uniaxial Bouc–Wen model (Bouc 1967; Wen 1976), Park et al. (1986) proposed a biaxial hysteretic model with shape parameter n=2 to account for the biaxial interaction. Wang and Wen (2000) further extended the biaxial model with n>2. According to this biaxial hysteretic model, the generalized restoring forces F_{sx} and F_{sy} are expressed as

$$F_{sx} = \alpha_x K_x q_x + (1 - \alpha_x) K_x z_x \tag{5a}$$

$$F_{sv} = \alpha_v K_v q_v + (1 - \alpha_v) K_v z_v \tag{5b}$$

$$\dot{z}_x = A_x \dot{q}_x - z_x I \tag{6a}$$

$$\dot{z}_{y} = A_{y}\dot{q}_{y} - z_{y}I \tag{6b}$$

$$I = |\dot{q}_{x}||z_{x}|^{n-1} [\beta_{0} + \gamma_{0} \operatorname{sgn}(\dot{q}_{x}z_{x})] / \Delta_{x}^{n} + |\dot{q}_{y}||z_{y}|^{n-1} [\beta_{0} + \gamma_{0} \operatorname{sgn}(\dot{q}_{y}z_{y})] / \Delta_{y}^{n}$$
 (6c)

where α_x and α_y = second (postyielding) stiffness ratios; z_x and z_y = hysteretic displacements; $\operatorname{sgn}(\cdot)$ = sign function; $A_x = A_y = 1$ in general; and Δ_x and Δ_y are yield displacements under uniaxial loads in x and y directions, respectively. The shape parameter n determines the smoothness of transition from preyielding to postyielding region; $\beta_0 + \gamma_0 = 1$, and often $\beta_0 = \gamma_0 = 0.5$. This biaxial model is referred to as Model 1 in the following discussion.

To better understand the biaxial hysteretic force model, the displacement q_0 and hysteretic displacement z_0 for a displacement path along Θ -axis, defined by a line passing the origin in the q_x/Δ_x and q_y/Δ_y plane with a selected counterclockwise rotation angle θ from the q_x/Δ_x , are considered (Lee and Hong 2010). As $q_x/\Delta_x = q_0\cos\theta$, $q_y/\Delta_y = q_0\sin\theta$, $z_x/\Delta_x = z_0\cos\theta$, $z_y/\Delta_y = z_0\sin\theta$, $A_x = A_y = A_0$, Eq. (6a) becomes

$$\dot{z}_0 = A_0 \dot{q}_0 - z_0 I_0 \tag{7a}$$

$$I_0 = |\dot{q}_0||z_0|^{n-1} [\beta_0 + \gamma_0 \text{sgn}(\dot{q}_0 z_0)](|\cos^n \theta| + |\sin^n \theta|)$$
 (7b)

The normalized yield displacement along the Θ -axis, $\Delta_0(\theta) = |z_{0u}(\theta)|$, is obtained by setting $\dot{z}_0 = 0$, and same sign for \dot{q}_0 and z_0 (Lee and Hong 2010) as

$$\Delta_0(\theta) = |z_{0u}(\theta)| = [|\cos^n \theta| + |\sin^n \theta|]^{-\frac{1}{n}}$$
(8)

It is evident that the yield surface, $\Delta_0(\theta)$ as a function of direction angle θ , is a circle, that is, isotropic, when n=2, indicating equal interaction of two directions. Otherwise, the normalized yield displacement depends on direction. When n=1, it becomes a rhombus, which indicates strong interaction in two directions. When $n \geq 5$, it approaches to a square, where the effect of interaction can be ignored.

The yield displacements and corresponding restoring forces in two directions are

$$\Delta_{\mathbf{r}}(\theta) = \Delta_{\mathbf{0}}(\theta)\cos\theta; \qquad \Delta_{\mathbf{v}}(\theta) = \Delta_{\mathbf{0}}(\theta)\sin\theta \qquad (9a)$$

$$F_{sx} = K_x \Delta_x(\theta); \qquad F_{sy} = K_y \Delta_y(\theta)$$
 (9b)

The normalized peak displacement $\mu_{\rm max}$ under biaxial wind loads, referred to as peak ductility demand, is defined (e.g., Lee and Hong 2010) as follows:

$$\mu_{\text{max}} = \max_{\text{For all } t} [|q_x(t)/\Delta_x|^n + |q_y(t)/\Delta_y|^n]^{\frac{1}{n}}$$
 (10)

An alternative generalization of the biaxial hysteresis model that can retain the isotropy and still allow for $n \neq 2$ was proposed by Harvey and Gavin (2014), which is referred to as Model 2 in the following discussion, and is as follows:

$$I = \{|\dot{q}_{x}||z_{x}|[\beta_{0} + \gamma_{0}\mathrm{sgn}(\dot{q}_{x}z_{x})]/\Delta_{x}^{2} + |\dot{q}_{y}||z_{y}|[\beta_{0} + \gamma_{0}\mathrm{sgn}(\dot{q}_{y}z_{y})]/\Delta_{y}^{2}\} \times [(z_{x}/\Delta_{x})^{2} + (z_{y}/\Delta_{y})^{2}]^{\frac{n-2}{2}}$$

$$(11)$$

Clearly, it corresponds to a circular normalized yield surface, i.e., $\Delta_0(\theta)=1$. Both models give the same relations under uniaxial loads but different models under biaxial loads. When n=2, both models are identical. Both models are used and discussed in this study.

Eqs. (4a)–(6a) can be incorporated into a state-space form as

$$\dot{\mathbf{v}} = \mathbf{g}(\mathbf{v}) + \mathbf{D}\mathbf{Q} \tag{12a}$$

$$\mathbf{v} = \begin{bmatrix} q_x \\ q_y \\ \dot{q}_x \\ \dot{q}_y \\ z_x \\ z_y \end{bmatrix}; \qquad \mathbf{g}(\mathbf{v}) = \begin{bmatrix} \dot{q}_x \\ \dot{q}_y \\ -\alpha_x \omega_x^2 q_x - 2\zeta_x \omega_x \dot{q}_x - (1 - \alpha_x) \omega_x^2 z_x \\ -\alpha_y \omega_y^2 q_y - 2\zeta_y \omega_y \dot{q}_y - (1 - \alpha_y) \omega_y^2 z_y \\ A_x \dot{q}_x - z_x I \\ A_y \dot{q}_y - z_y I \end{bmatrix}; \qquad \text{equations of motion can be expressed in the following not sional form:} \\ q_x^{*\prime\prime} + 2\zeta_x q_x^{*\prime} + \alpha_x q_x^* + (1 - \alpha_x) z_x^* = Q_x^* \\ q_y^{*\prime\prime} + 2\zeta_y q_y^{*\prime} R_\omega + \alpha_y R_\omega^2 q_y^* + (1 - \alpha_y) R_\omega^2 z_y^* = R_\omega^2 Q_y^* \\ z_x^{*\prime} = q_x^{*\prime} - z_x^* I^* \end{bmatrix}$$

$$\mathbf{D} = \begin{bmatrix} 0 & 0 \\ 0 & 0 \\ M_x^{-1} & 0 \\ 0 & M_y^{-1} \\ 0 & 0 \\ 0 & 0 \end{bmatrix}; \qquad \mathbf{Q} = \begin{bmatrix} Q_x \\ Q_y \end{bmatrix}$$
 (12b)

The response time-history analysis can be carried out by using a step-by-step integration method or 4th-order Runge-Kutta

By introducing nondimensional parameters and variables, $t^* = \omega_x t; \ q_x^* = q_x/\Delta_x; \ q_y^* = q_y/\Delta_y; \ z_x^* = z_x/\Delta_x; \ z_y^* = z_y/\Delta_y;$ $()' = d()/dt^* = d()/dt/\omega_x;$ $()'' = d^2()/dt^{*2} = d^2()/dt^2/\omega_x^2;$ $Q_x^* = Q_x(t)/K_x/\Delta_x$; $Q_y^* = Q_y(t)/K_y/\Delta_y$; and $R_\omega = \omega_y/\omega_x$, the equations of motion can be expressed in the following nondimen-

$$q_x^{*\prime\prime} + 2\zeta_x q_x^{*\prime} + \alpha_x q_x^* + (1 - \alpha_x) z_x^* = Q_x^*$$
 (13a)

$$q_y^{*\prime\prime} + 2\zeta_y q_y^{*\prime} R_\omega + \alpha_y R_\omega^2 q_y^* + (1 - \alpha_y) R_\omega^2 z_y^* = R_\omega^2 Q_y^*$$
 (13b)

$$z_x^{*\prime} = q_x^{*\prime} - z_x^* I^* \tag{14a}$$

$$z_{y}^{*\prime} = q_{y}^{*\prime} - z_{y}^{*} I^{*} \tag{14b}$$

$$I^* = |q_x^{*\prime}||z_x^*|^{n-1} [\beta_0 + \gamma_0 \operatorname{sgn}(q_x^{*\prime} z_x^*)] + |q_y^{*\prime}||z_y^*|^{n-1} [\beta_0 + \gamma_0 \operatorname{sgn}(q_y^{*\prime} z_y^*)]$$
(14c)

It is obvious that the influencing nondimensional parameters are damping ratios ζ_x and ζ_y , frequency ratio $R_\omega = \omega_y/\omega_x$, hysteretic restoring force parameters β_0 and γ_0 , stiffness ratios α_x and α_y , and normalized generalized forces $Q_x^*(t^*)$ and $Q_y^*(t^*)$.

Time-Varying Mean Displacement

The inelastic displacement has a time-varying mean component that is governed by the following equations, which can be obtained by taking expectation on both sides of Eq. (12a):

$$\dot{\boldsymbol{\mu}}_{\boldsymbol{\nu}} = \boldsymbol{g}(\boldsymbol{\mu}_{\boldsymbol{\nu}}) + \boldsymbol{D}\boldsymbol{\mu}_{\boldsymbol{O}} \tag{15a}$$

$$\mu_{\mathbf{v}} = \begin{bmatrix} \mu_{q_{x}} \\ \mu_{q_{y}} \\ \mu_{\dot{q}_{x}} \\ \mu_{\dot{q}_{y}} \\ \mu_{z_{x}} \\ \mu_{z_{y}} \end{bmatrix}; \qquad \mathbf{g}(\mu_{\mathbf{v}}) = \begin{bmatrix} \mu_{\dot{q}_{x}} \\ \mu_{\dot{q}_{y}} \\ -\alpha_{x}\omega_{x}^{2}\mu_{q_{x}} - 2\zeta_{x}\omega_{x}\mu_{\dot{q}_{x}} - (1 - \alpha_{x})\omega_{x}^{2}\mu_{z_{x}} \\ -\alpha_{y}\omega_{y}^{2}\mu_{q_{y}} - 2\zeta_{y}\omega_{y}\mu_{\dot{q}_{y}} - (1 - \alpha_{y})\omega_{y}^{2}\mu_{z_{y}} \\ \mu_{\dot{q}_{x}} - \beta_{0}E_{x1}/\Delta_{x}^{n} - \gamma_{0}E_{x2}/\Delta_{x}^{n} - \beta_{0}E_{x3}/\Delta_{y}^{n} - \gamma_{0}E_{x4}/\Delta_{y}^{n} \\ \mu_{\dot{q}_{y}} - \beta_{0}E_{y1}/\Delta_{x}^{n} - \gamma_{0}E_{y2}/\Delta_{x}^{n} - \beta_{0}E_{y3}/\Delta_{y}^{n} - \gamma_{0}E_{y4}/\Delta_{y}^{n} \end{bmatrix}; \qquad \mu_{\mathbf{Q}} = \begin{bmatrix} \mu_{\mathbf{Q}_{x}} \\ \mu_{\mathbf{Q}_{y}} \end{bmatrix}$$
(15b)

$$E_{x1} = E[|\dot{q}_x||z_x|^{n-1}z_x]; \qquad E_{x2} = E[\dot{q}_x|z_x|^n]; E_{x3} = E[z_x|\dot{q}_y||z_y|^{n-1}]; \qquad E_{x4} = E[z_x\dot{q}_y|z_y|^{n-1}\operatorname{sgn}(z_y)]$$
(15c)

$$\begin{split} E_{y1} &= E[z_y |\dot{q}_x| |z_x|^{n-1}]; \qquad E_{y2} = E[z_y \dot{q}_x |z_x|^{n-1} \mathrm{sgn}(z_x)]; \\ E_{y3} &= E[|\dot{q}_y| |z_y|^{n-1} z_y]; \qquad E_{y4} = E[\dot{q}_y |z_y|^n] \end{split} \tag{15d}$$

where $\mu_{\nu} = E(\nu)$ and $\mu_{O} = E(Q)$ are mean values of ν and Q; and $E(\cdot)$ is expectation operator. Here, the biaxial hysteretic Model 1 is adopted, while similar expressions can be given for Model 2.

By assuming the responses follow joint Gaussian distributions, the linearization coefficients E_{xi} and E_{vi} (i = 1 - 4) can be expressed in terms of first two statistical moments-i.e., mean, variance and covariance of the responses (Appendix I). The timevarying mean can be calculated from Eq. (15a) using a step-by-step integration method or Runge-Kutta method. The time-varying variance and covariance approach to the steady-state time-invariant values very fast. For the estimation of time-varying mean response, the steady-state variance and covariance can be used (Feng and Chen 2018). The including of the mean load effect is simply to shift the average center position of restoring force and displacement loop to a new position, but not to change the shape of the loop. Therefore, the inelastic dynamic response around the time-varying mean is not affected by the mean loads, and thus can be estimated first with zero mean load (Roberts and Spanos 2003; Feng and Chen 2018; Huang and Chen 2022).

The steady-state mean can be determined by setting $\dot{\mu}_{\nu} = 0$, which leads to

$$\alpha_x K_x \mu_{a_x} + (1 - \alpha_x) K_x \mu_{z_x} = \mu_{O_x} \tag{16a}$$

$$\alpha_{\mathbf{y}} K_{\mathbf{y}} \mu_{q_{\mathbf{y}}} + (1 - \alpha_{\mathbf{y}}) K_{\mathbf{y}} \mu_{z_{\mathbf{y}}} = \mu_{Q_{\mathbf{y}}}$$

$$\tag{16b}$$

$$\beta_x E_{x1} + \gamma_x E_{x2} + \beta_y E_{x3} + \gamma_y E_{x4} = 0 \tag{16c}$$

$$\beta_x E_{v1} + \gamma_x E_{v2} + \beta_v E_{v3} + \gamma_v E_{v4} = 0 \tag{16d}$$

where $\beta_x = \beta_0/\Delta_x^n$, $\gamma_x = \gamma_0/\Delta_x^n$, $\beta_y = \beta_0/\Delta_y^n$, and $\gamma_y = \beta_0/\Delta_y^n$. It can be proved that $\mu_{z_x} = \mu_{z_y} = 0$ is a sufficient condition for Eqs. (16c) and (16d). It is also believed to be a necessary condition. Subsequently, we have

$$\mu_{q_x} = \frac{\mu_{Q_x}}{\alpha_x K_x}; \qquad \mu_{q_y} = \frac{\mu_{Q_y}}{\alpha_y K_y} \tag{17}$$

which indicates that the steady-state mean response in each direction is determined by the respective static load and second stiffness. Consider the case where $\mu_{Q_x}=0$, we have $\mu_{z_x}=0$, $\mu_{q_x}=0$, $\mu_{\dot{q}_x}=0$. Eq. (15a) is simplified as

$$\dot{\boldsymbol{\mu}}_{\boldsymbol{\nu}_{\boldsymbol{\nu}}} = \boldsymbol{g}(\boldsymbol{\mu}_{\boldsymbol{\nu}_{\boldsymbol{\nu}}}) + \boldsymbol{D}_{0\boldsymbol{y}}\boldsymbol{\mu}_{Q_{\boldsymbol{\nu}}} \tag{18a}$$

$$\boldsymbol{\mu}_{\mathbf{v}_{y}} = \begin{bmatrix} \mu_{q_{y}} \\ \mu_{\dot{q}_{y}} \\ \mu_{z_{y}} \end{bmatrix}; \quad \boldsymbol{g}(\boldsymbol{\mu}_{\mathbf{v}_{y}}) = \begin{bmatrix} \mu_{\dot{q}_{y}} \\ -\alpha_{y}\omega_{y}^{2}\mu_{q_{y}} - 2\zeta_{y}\omega_{y}\mu_{\dot{q}_{y}} - (1-\alpha_{y})\omega_{y}^{2}\mu_{z_{y}} \\ \mu_{\dot{q}_{y}} - \beta_{0}E_{y1}/\Delta_{x}^{n} - \gamma_{0}E_{y2}/\Delta_{x}^{n} - \beta_{0}E_{y3}/\Delta_{y}^{n} - \gamma_{0}E_{y4}/\Delta_{y}^{n} \end{bmatrix}; \quad \boldsymbol{D}_{0y} = \begin{bmatrix} 0 \\ M_{y}^{-1} \\ 0 \end{bmatrix}$$
(18b)

It is evident that the time-varying mean response in y direction with nonzero mean load is affected by variance and covariance of responses in both x and y directions.

Statistical Linearization Approach for Fluctuating Response

The variance and covariance of dynamic responses can be estimated under dynamic wind loads with zero mean, and are considered time-invariant (Feng and Chen 2018). The hysteretic velocity \dot{z}_x and \dot{z}_y in Eq. (6a) are linearized as

$$\dot{z}_x = C_{x1}\dot{q}_x + C_{x2}\dot{q}_y + C_{x3}z_x + C_{x4}z_y \tag{19a}$$

$$\dot{z}_{v} = C_{v1}\dot{q}_{x} + C_{v2}\dot{q}_{v} + C_{v3}z_{x} + C_{v4}z_{v} \tag{19b}$$

$$C_{x1} = E\left[\frac{\partial \dot{z}_x}{\partial \dot{q}_x}\right]; \qquad C_{x2} = E\left[\frac{\partial \dot{z}_x}{\partial \dot{q}_y}\right];$$

$$C_{x3} = E\left[\frac{\partial \dot{z}_x}{\partial z_x}\right]; \qquad C_{x4} = E\left[\frac{\partial \dot{z}_x}{\partial z_y}\right]$$
(19c)

$$C_{y1} = E\left[\frac{\partial \dot{z}_{y}}{\partial \dot{q}_{x}}\right]; \qquad C_{y2} = E\left[\frac{\partial \dot{z}_{y}}{\partial \dot{q}_{y}}\right];$$

$$C_{y3} = E\left[\frac{\partial \dot{z}_{y}}{\partial z_{x}}\right]; \qquad C_{y4} = E\left[\frac{\partial \dot{z}_{y}}{\partial z_{y}}\right]$$
(19d)

where the responses \dot{q}_x , \dot{q}_y , z_x , and z_y are assumed to follow jointly Gaussian distributions. The coefficients C_{xi} and C_{yi} (i=1-4) can be further expressed in terms of the variance and covariance of responses (Appendix II).

The equations of motion are then written as

$$\dot{\mathbf{v}} = \mathbf{B}\mathbf{v} + \mathbf{D}\mathbf{Q} \tag{20a}$$

$$\mathbf{B} = \begin{bmatrix} 0 & 0 & 1 & 0 & 0 & 0 \\ 0 & 0 & 0 & 1 & 0 & 0 \\ -\alpha_x \omega_x^2 & 0 & -2\zeta_x \omega_x & 0 & -(1-\alpha_x)\omega_x^2 & 0 \\ 0 & -\alpha_y \omega_y^2 & 0 & -2\zeta_y \omega_y & 0 & -(1-\alpha_y)\omega_y^2 \\ 0 & 0 & C_{x1} & C_{x2} & C_{x3} & C_{x4} \\ 0 & 0 & C_{y1} & C_{y2} & C_{y3} & C_{y4} \end{bmatrix}$$
 (20b)

Accordingly, the response variance and covariance are computed via spectral analysis as

$$S_{\mathbf{v}}(\omega) = H_{\mathbf{v}}(\omega)S_{\mathbf{O}}(\omega)H_{\mathbf{v}}^{*T}(\omega)$$
 (21)

$$\boldsymbol{H}_{\mathbf{v}}(\omega) = (i\omega \boldsymbol{I} - \boldsymbol{B})^{-1}\boldsymbol{D} \tag{22}$$

$$\mathbf{R}_{\nu} = \text{cov}[\nu \nu^{\mathrm{T}}] = \int_{0}^{\infty} \mathbf{S}_{\nu}(\omega) d\omega \tag{23}$$

where R_{ν} = covariance matrix; $S_{Q}(\omega)$ and $S_{\nu}(\omega)$ = one-side power spectra density (PSD) matrices of Q and ν ; I = identity matrix; $\omega = 2\pi f$; $i = \sqrt{-1}$; and * and T = complex conjugate and matrix transpose operators. An iteration is needed as the statistical linearization coefficients involve the unknown response statistics.

Nonlinear FE Building Model and Wind Loads

Nonlinear FE Building Model

A 60-story high-rise steel building 182.88-m high, 45.72-m wide, and 30.48-m deep is considered (Fig. 2). The building has an outrigger system at three elevations (20th and 21st, 40th and 41st, and 60th floors) and a core bracing system to resist the lateral load. The building frame consists of 2,100 columns, 3,480 beams, and 2,560 diagonal bracings, including a total of 16 types of member sections. All members were modeled in fiber-type models (NIST 2017) and each element has five fiber sections. More than 300 fibers over each column and bracing cross-sectional area and more than 150 fibers over each beam cross-sectional area were used. The nonlinearity of the steel material is described by a bilinear model with a yield stress of 345 MPa and a postyielding stiffness ratio 0.01. The fundamental frequencies in two translational directions are

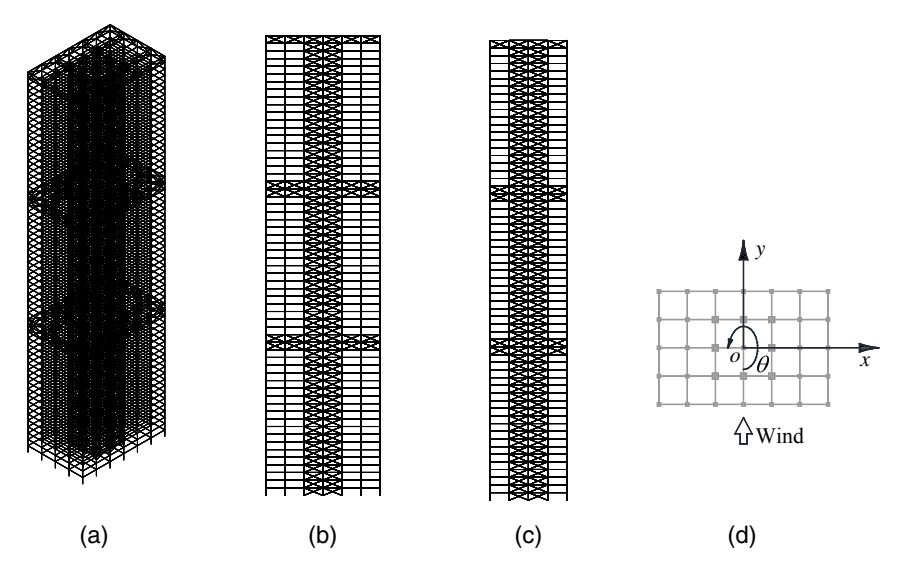


Fig. 2. FE model of the building frame: (a) 3D view; (b) front view; (c) side view; and (d) plain view.

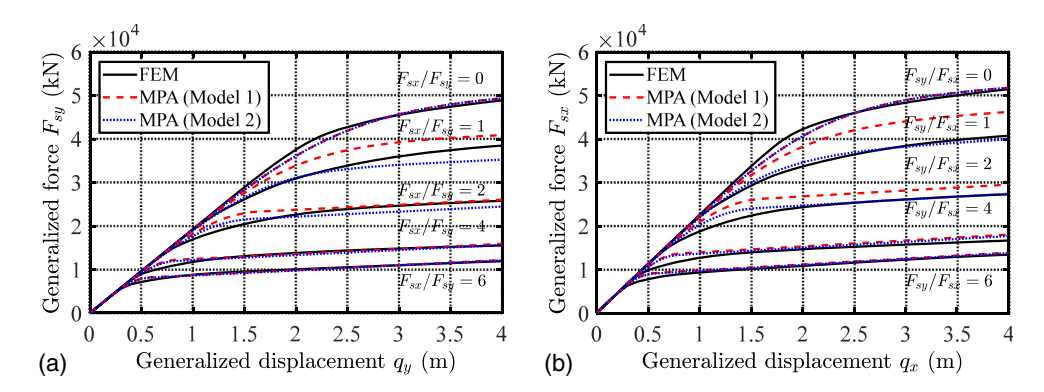


Fig. 3. Generalized restoring force and deformation relations: (a) alongwind (y); and (b) crosswind (x).

 $f_x = 0.173$ Hz and $f_y = 0.164$ Hz. The modal damping ratios are assumed to be $\zeta_x = \zeta_y = 1\%$. More detailed information about the FE model can be found in Park and Yeo (2018) and Huang and Chen (2022).

Fig. 3 shows the generalized restoring force-deformation relations for given ratio F_{sv}/F_{sx} , where $F_{sv}/F_{sx} = 0$ and $F_{sx}/F_{sv} =$ 0 correspond to the cases of uniaxial load in x and y directions, respectively. The uniaxial hysteretic models are fitted for both directions with n=4, $\alpha_x=\alpha_y=0.06$, $\Delta_x=2.2$ m, and $\Delta_y=$ 2.5 m. For a given ratio F_{sy}/F_{sx} , the generalized restoring forcedisplacement relation in each direction is fitted into a uniaxial hysteretic model from which the yield displacements are determined, denoted as $\Delta_x(\theta)$ and $\Delta_y(\theta)$, respectively, for x and y directions. The corresponding direction is defined as $\theta = \arctan\{[\Delta_v(\theta)/\Delta_v]/$ $[\Delta_x(\theta)/\Delta_x]$, which is also $\theta = \arctan\{[F_{sy}/K_y/\Delta_y(\theta)]/[F_{sx}/K_y/\Delta_y(\theta)]\}$ $K_x/\Delta_x(\theta)$. With this information, the yield displacement boundary is constructed as shown in Fig. 4, which is compared with those from biaxial Models 1 and 2. The yield displacement boundary is close to a circle and close to that of Model 2. It is evident that the yield displacement in one direction declines due to the increase of the load in another direction. The hysteretic relations of the generalized forces and displacements represent the global behavior of the building, and are less sensitive to the material model used in the FE model. On the other hand, the local plasticity of building members will be affected by the material model. It should be noted that the P-Delta effect, effects of strength deterioration,

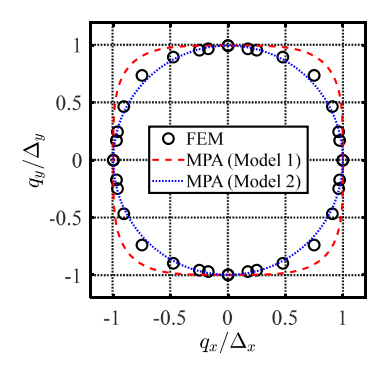


Fig. 4. Yield surfaces of the hysteresis models.

and stiffness degradation are not considered in current study but will be investigated in future work.

Wind Loading Model

The alongwind static wind force at ith story is determined as

$$\bar{P}_i = 0.5 \rho U_H^2 \bar{C}_D B H_0 \left(\frac{z_i}{H}\right)^{2\alpha_s} \tag{24}$$

where ρ = air density, 1.22 kg/m³; U_H = mean wind speed at the building top averaged in 10 min; B = building width; H_0 = story

height and $H_0=3.048$ m; H= building height; $z_i=$ elevation of ith floor above the ground; $\bar{C}_D=$ constant drag force coefficient and is determined from the static coefficient of base bending moment \bar{C}_M as $\bar{C}_D=2\bar{C}_M(\alpha_s+1)$; and $\alpha_s=0.2$ is the power law exponent of the wind speed profile for the suburban terrain.

The cross power spectral density (CPSD) function of *i*th and *j*th story forces in alongwind direction is given (Chen and Kareem 2005c) as follows:

$$S_{P_i P_j}(f) = S_{P_0}(f) \left(\frac{z_i}{H}\right)^{\alpha_s} \left(\frac{z_j}{H}\right)^{\alpha_s} \exp\left(-\frac{k_y f H}{U_H} \frac{|z_i - z_j|}{H}\right) \quad (25)$$

$$S_{P_0}(f) = \left(\frac{1}{2}\rho U_H^2 B H_0\right)^2 S_{C_M}(f) / |J_z(f)|^2$$
 (26)

$$|J_z(f)|^2 = \left(\frac{H_0}{H}\right)^2 \sum_{i=1}^N \sum_{j=1}^N \left(\frac{z_i}{H}\right)^{\alpha_s + 1} \left(\frac{z_j}{H}\right)^{\alpha_s + 1}$$

$$\times \exp\left(-\frac{k_y f H}{U_H} \frac{|z_i - z_j|}{H}\right) \tag{27}$$

where $S_{C_M}(f)$ = power spectrum of the base bending moment coefficient $C_M(t)$; N = number of stories; and k_y = 7 is the decay factor for the alongwind load. The same CPSD model is also used for crosswind story forces, but different spectrum $S_{C_M}(f)$ and decay factor k_y = 5 are adopted. The crosswind story forces have stronger heightwise correlation/coherence. The power spectrum of the crosswind base bending moment coefficient features a peak at the vortex-shedding frequency.

The power spectra of alongwind and crosswind base bending moment coefficients are given according to the recommendations of the Architectural Institute of Japan (AIJ 2004; Ding and Chen 2015). The STD of alongwind C_M is $\sigma_{C_M} = 0.11$. For the crosswind, $\sigma_{C_M} = 0.1175$; the bandwidth parameter of the spectrum takes $\beta_1 = 0.28$; parameter $\kappa_1 = 0.85$; and the Strouhal number $S_t = 0.09$.

The alongwind and crosswind loadings are assumed to be independent thus are simulated independently based on the power spectral models using the spectral representation method (Shinozuka and Jan 1972; Chen and Kareem 2005c). The torsional wind load and response are quite low, and thus are not considered in this study. It should be noted that, when other wind directions are of concern, the alongwind and crosswind loadings will have a certain level of correlation/coherence, which can be readily considered in the simulation with a newly introduced coherence model. The correlation of building responses in two principal directions is affected by modal frequencies and damping ratios and coherence/ correlation of the generalized forces, and is lower than the correlation of generalized forces (Chen and Kareem 2005a, b). The responses can be statistically independent even under strongly correlated wind loadings when building modal frequencies in two principal directions are well separated. The correlation of inelastic alongwind and crosswind responses is also affected by their yielding levels that change the building dynamic properties in two directions. When the hysteretic forces are described in the uniaxial model, the alongwind and crosswind responses can be computed separately.

Verification of Reduced-Order Building Model

Statistics of Fluctuating Response

The accuracy of the reduced-order building model with hysteretic restoring forces (MPA approach) is examined through response history analysis and comparison with the results from the high-fidelity nonlinear FE model with distributed plasticity. Both linear and nonlinear responses with zero mean wind load are computed for comparison. The 10-min mean wind speed at the building top varies from 40 to 80 m/s. The response time-history is computed using the Runge–Kutta method. The building is assumed to be at rest at beginning. The response statistics at a given wind speed are computed from 10 response-history samples through ensemble average. For each sample, the time step is 0.04 s and the duration is 900 s. The time-history at the first 300 s is removed in analysis to avoid the transient effect.

Fig. 5 shows time history samples of the building top displacements in both alongwind and crosswind directions calculated from the FE model, and the MPA with hysteretic Model 1 and 2 under biaxial loads without mean alongwind load. Fig. 6 portrays the STDs of the alongwind building top displacement and acceleration, peak factor, and kurtosis of the displacement. Fig. 7 is the result for crosswind response. It is evident that three analyses yield fairly close estimations. The errors in the estimated STDs of alongwind response from these two hysteretic models are less than 7%. The errors in the crosswind response are less than 11%. The inelastic response is lower than the corresponding elastic response attributed to the effect of additional hysteretic damping. For instance, according to the analysis using the FE model, the alongwind displacement and acceleration at $U_H = 80 \text{ m/s}$ are reduced by 26% and 32%, respectively. The crosswind displacement and acceleration are reduced by 55%. The probability distribution of fluctuating alongwind displacement is close to Gaussian distribution with a kurtosis close to 3, and the peak factor is close to that estimated by the Davenport formula (Davenport 1964). The inelastic crosswind response at higher wind speeds corresponds to higher ductility factor or higher level of yielding and shows hardening non-Gaussian distribution with kurtosis less than 3 and a reduced peak factor.

Figs. 8 and 9 display the response statistics under uniaxial loads. Both biaxial hysteretic models are reduced to an identical uniaxial model. It is confirmed that predictions from hysteretic models are very close to those from FE modeling. Fig. 10 shows the ratios of STDs of building top displacement and acceleration under biaxial and uniaxial loads from the FE model. It is evident that the crosswind response, which is larger than alongwind response, remains almost unaffected, while the alongwind response is reduced under the action of biaxial loads when the ductility demand of crosswind response is high, which is attributed to the increase in additional hysteretic damping.

Fig. 11 shows the peak ductility demands that increase with increasing wind speed. Because the crosswind response is much higher than the alongwind response, the ductility demand is dominated by the crosswind response, remaining almost unchanged under uniaxial and biaxial loads.

The correlation coefficient between alongwind and crosswind displacements at building top was also calculated at different wind speeds under both uniaxial and biaxial loads. The correlation coefficient is less than 0.05, and thus both can be considered as mutually independent.

Influence of Hysteretic Model

The RHA is also carried out using hysteretic Model 1 with the shape parameter n=4 replaced by n=2 for both directions, while other parameters remain the same. The generalized restoring force-deformation relations for Model 1 with n=2 and 4 and FE model are plotted in Fig. 12. The hysteretic model with n=2 corresponds to wider and smoother transition from elastic to plastic regions. The yielding boundary of the biaxial model becomes a circle.

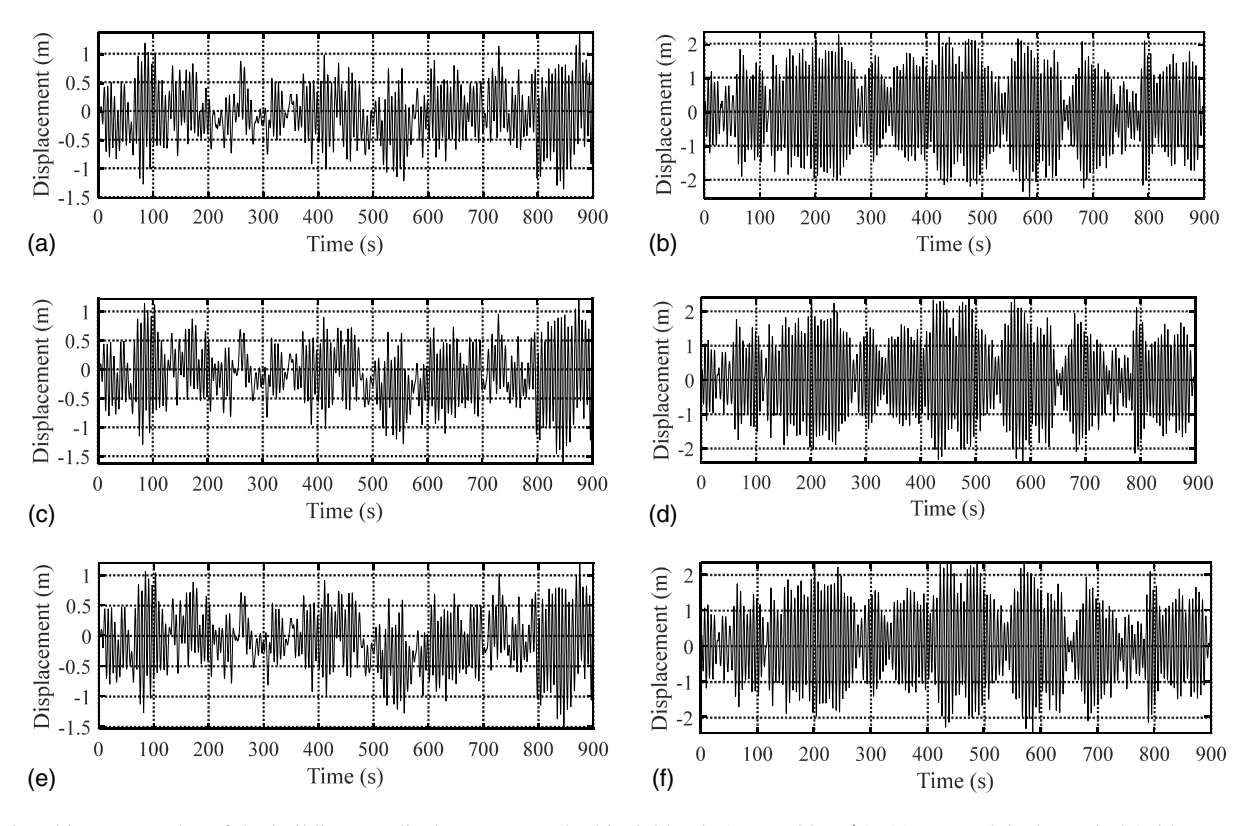


Fig. 5. Time-history samples of the building top displacements under biaxial loads ($U_H = 80 \text{ m/s}$): (a) FE model, alongwind (without mean load); (b) FE model, crosswind; (c) MPA (Model 1), alongwind (without mean load); (d) MPA (Model 1), crosswind; (e) MPA (Model 2), alongwind (without mean load); and (f) MPA (Model 2), crosswind.

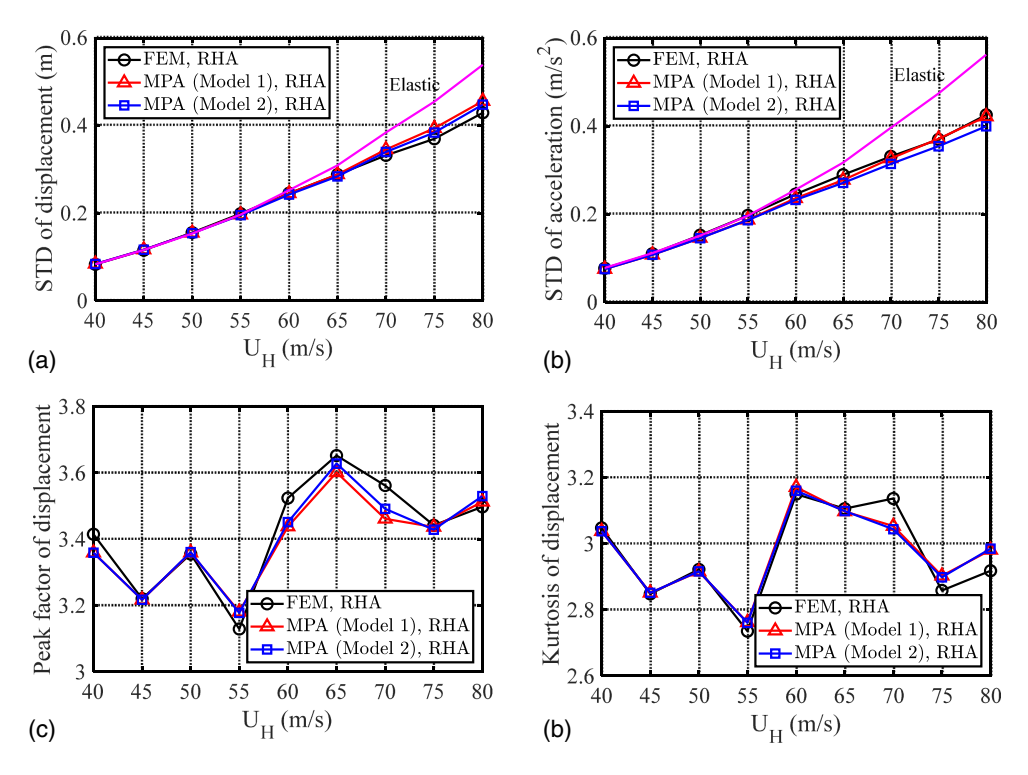


Fig. 6. Statistics of alongwind response under different wind speeds under biaxial loads: (a) STD of displacement; (b) STD of acceleration; (c) peak factor of displacement; and (d) kurtosis of displacement.

The estimated STDs of alongwind and crosswind responses are presented in Fig. 13. The response power spectra are also compared in Fig. 14. It is evident that the model with n=2 leads to increased level of yielding and larger hysteretic damping,

thus reduced response. The reductions in alongwind acceleration, crosswind displacement, and acceleration are larger than alongwind displacement. The power spectrum of alongwind displacement indicates that there is noticeable low-frequency

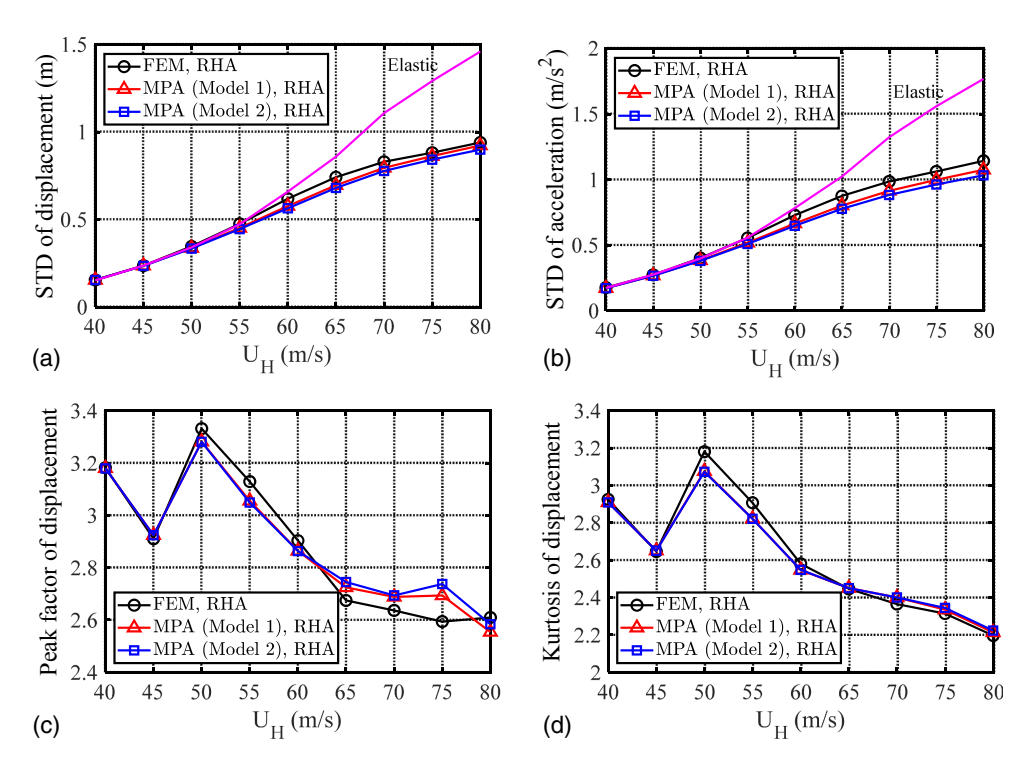


Fig. 7. Statistics of crosswind response under different wind speeds under biaxial loads: (a) STD of displacement; (b) STD of acceleration; (c) peak factor of displacement; and (d) kurtosis of displacement.

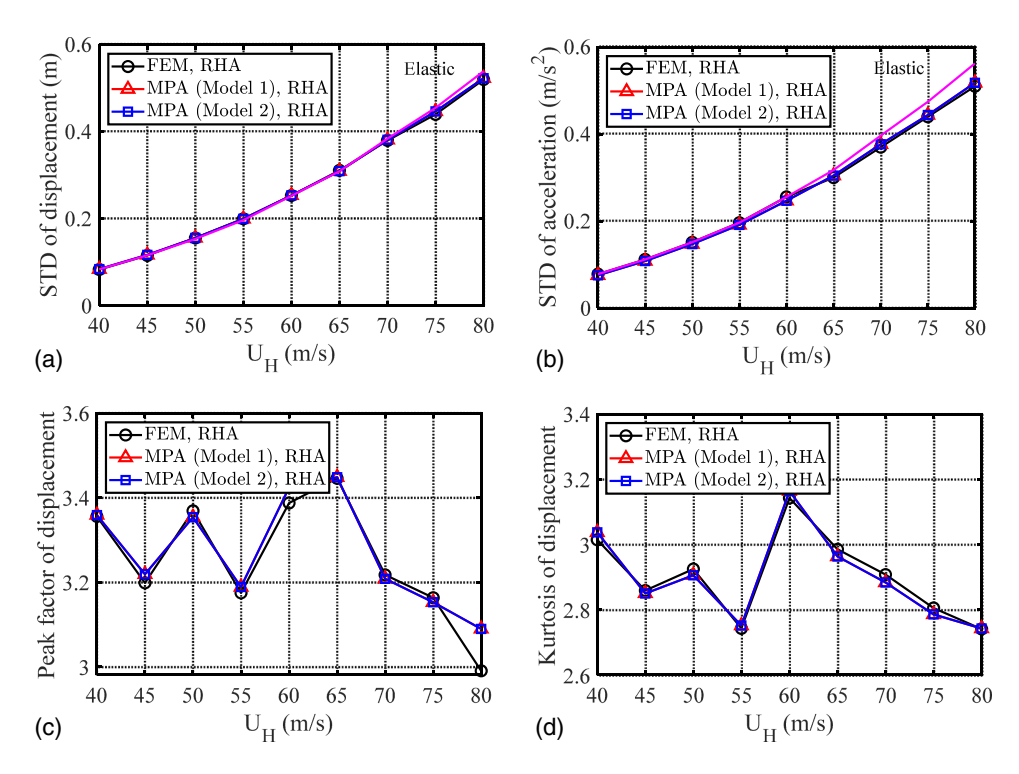


Fig. 8. Statistics of alongwind response under different wind speeds under uniaxial loads: (a) STD of displacement; (b) STD of acceleration; (c) peak factor of displacement; and (d) kurtosis of displacement.

background drift at higher wind speed in the case of n=2, which contributes to less reduction of alongwind displacement due to yielding. This low-frequency drift is not observed in crosswind displacement, which has even higher ductility demand. It also does not exist in alongwind and crosswind accelerations.

The alongwind displacement predicted from the FE model does not have such a low-frequency drift at this low level of yielding.

It has been known that the Bouc-Wen hysteretic model is one of the endochronic models that exhibits displacement drift, force

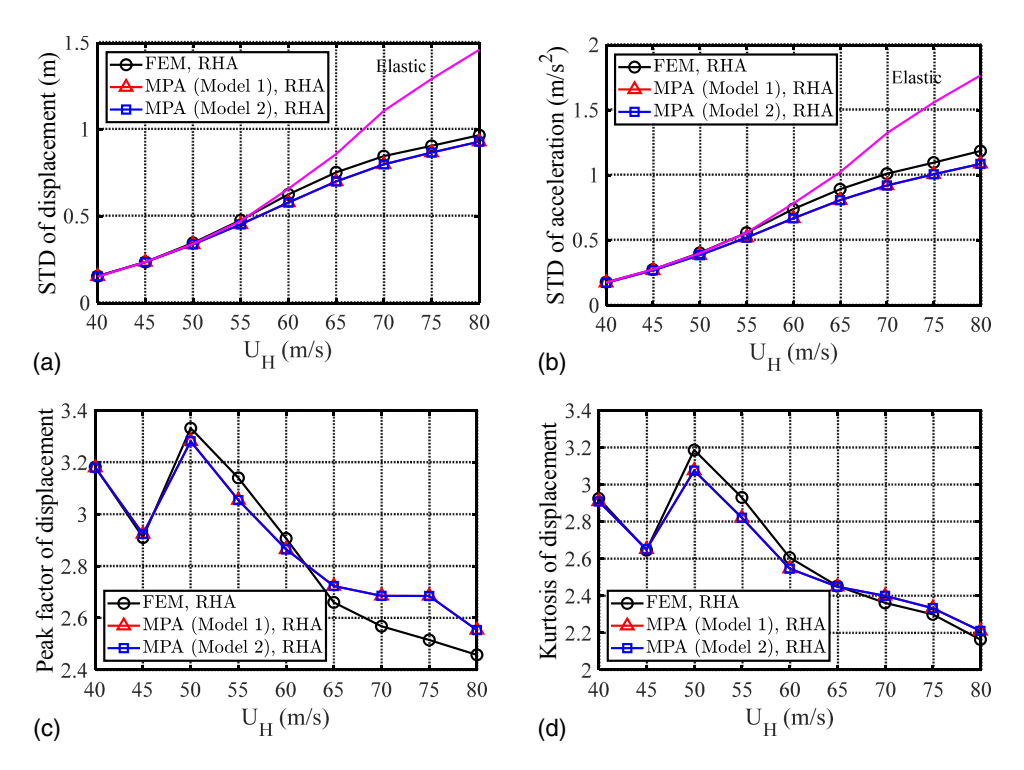


Fig. 9. Statistics of crosswind response under different wind speeds under uniaxial loads: (a) STD of displacement; (b) STD of acceleration; (c) peak factor of displacement; and (d) kurtosis of displacement.

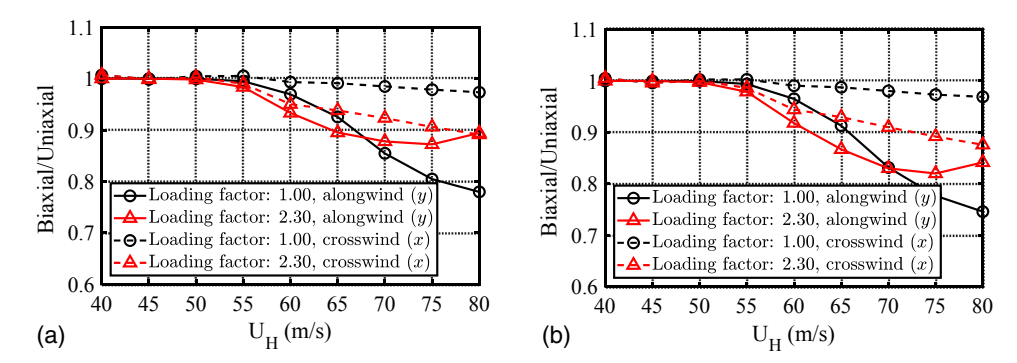


Fig. 10. Influence of biaxial interaction on alongwind and crosswind responses: (a) displacement; and (b) acceleration.

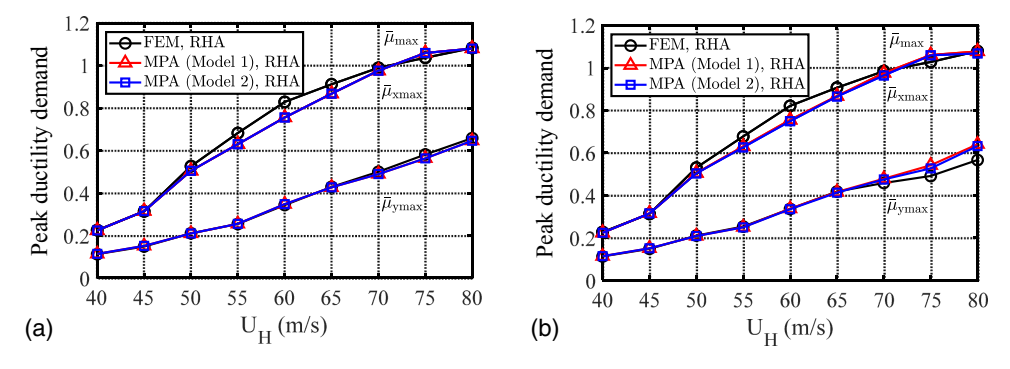


Fig. 11. Peak ductility demands of building top displacements: (a) uniaxial loads; and (b) biaxial loads.

relaxation, and nonclosure of hysteretic loops when subjected to short unloading–reloading paths, thus locally violates Drucker's postulate of plasticity (Thyagarajan 1989; Wong et al. 1994; Charalampakis and Koumousis 2009). This effect is more noticeable

when the shape parameter n and postyielding stiffness ratio are low. The alongwind loading has higher low-frequency energy, thus the alongwind displacement is susceptible to drift. Clearly, the hysteretic model with n=4 gives better estimations.

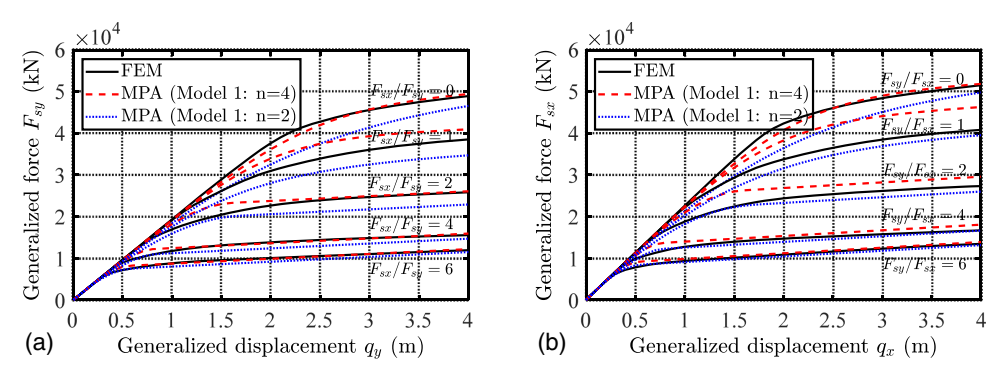


Fig. 12. Comparison of generalized restoring force and deformation relations: (a) MPA in alongwind (y); and (b) MPA in crosswind (x).

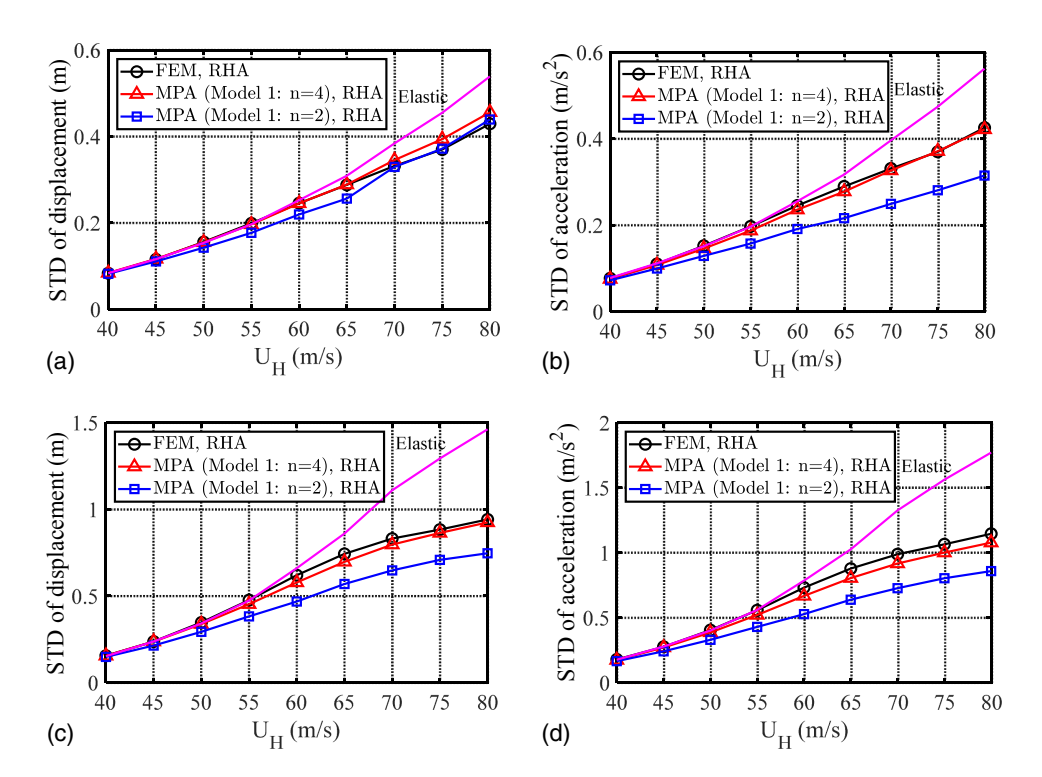


Fig. 13. STDs of responses influenced by hysteretic model: (a) alongwind displacement; (b) alongwind acceleration; (c) crosswind displacement; and (d) crosswind acceleration.

Time-Varying Mean Alongwind Displacement

Fig. 15 shows time-history samples of the alongwind building top displacement calculated from FE modeling and two hysteresis models with n=4 at $U_H=80$ m/s under both uniaxial and biaxial loads where the mean alongwind load is included. Fig. 16 shows the time-varying mean displacement estimated from ensemble average of 10 simulated samples at $U_H=60$ and 80 m/s. The two hysteretic models lead to much higher time-varying mean compared with that of FEM. This may be attributed to the difference in the postyielding stiffness and hysteretic restoring force-displacement relation in the transient region from linear elastic to postyielding states. A small difference in the very low postyielding stiffness can cause significant difference in the time-varying mean displacement. The accumulation of the difference at every step of calculation causes a great difference at the end of calculation with a longer duration. In future practice of building design, the

level of plasticity of building members will be limited such that the time-varying mean alongwind displacement will be much lower, and the difference between the predictions from the FE model and reduced-order model will be reduced. Future research work is needed to resolve the difference of predicted time-varying mean alongwind displacement. Nevertheless, the reduced-order model is very useful in predicting dynamic responses.

At higher wind speed, the yielding is more frequent, and thus the time-varying mean reaches its steady-state value more rapidly. The Model 2 with n=4 leads to slightly higher time-varying mean compared with Model 1 with n=4 under biaxial loads. Under uniaxial loads, both hysteretic models reduce to the same model and the time-varying mean alongwind displacement grows slower. The steady-state mean displacements under uniaxial and biaxial loadings are identical, which is determined by the mean wind load and postyielding stiffness. Similar results are also obtained at other wind speeds.

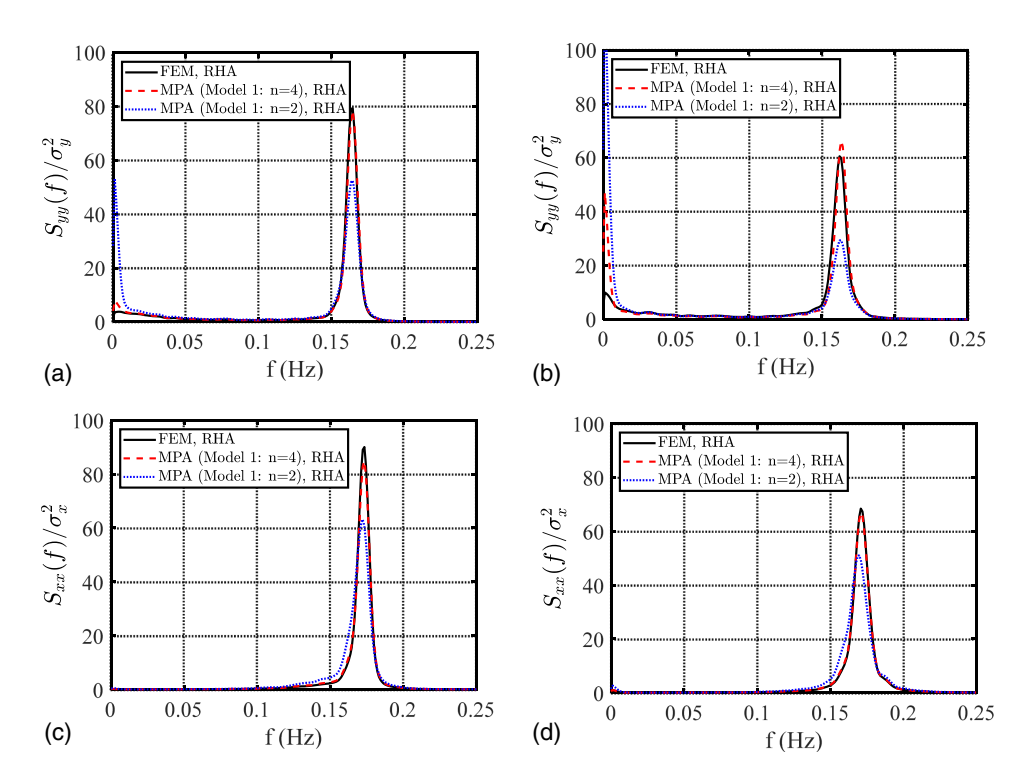


Fig. 14. PSDs of building top displacements: (a) alongwind displacement ($U_H = 60 \text{ m/s}$); (b) alongwind displacement ($U_H = 80 \text{ m/s}$); (c) crosswind displacement ($U_H = 60 \text{ m/s}$); and (d) crosswind displacement ($U_H = 80 \text{ m/s}$).

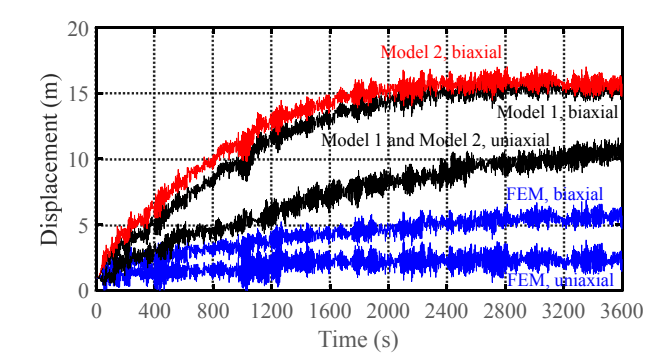


Fig. 15. Time-history samples of alongwind building top displacement $(U_H = 80 \text{ m/s})$.

Verification of Response Analysis Approach

Accuracy of Statistical Linearization Approach

The accuracy of the statistical linearization approach with hysteretic Model 1, n=2 and 4, is examined in Fig. 17 by comparing the results from RHA with n=4. The linearization approach with n=2 and 4 leads to very accurate estimation of alongwind response, which has a relatively lower level of yielding. For crosswind response at higher wind speed with relatively higher level of yielding, the linearization approach with n=4 underestimates the response. At $U_H=80$ m/s, the STD of crosswind displacement is underestimated by 12%. Use of n=2 results in slightly higher and better estimation with a difference less than 6% for crosswind displacement. Furthermore, the model with n=2 is easier to converge and is less sensitive to the assumption of Gaussian probability distribution of response. In fact, the probability distributions of hysteretic

displacements $z_x(t)$ and $z_y(t)$ are bounded and have peaks at positive and negative yield displacements. The crosswind building response also shows non-Gaussian distributions at higher wind speeds. The error introduced by assumption of Gaussian distribution is amplified when a larger value of n is used, as higher statistical moments that are more sensitive to the distribution tails are involved in the calculation. It should be mentioned that the statistical linearization approach with Gaussian response assumption is unable to further address the influence of non-Gaussian distribution on peak response. When the peak factor of Gaussian response is used, the hysteretic model with n=4 gives a better estimation of peak response.

The linearization with Model 2 and n=2 is identical to that of Model 1 with n=2. The linearization with Model 2 and n=4 does not have better performance, and thus is not further discussed. The accuracy of the statistical linearization approach for estimating response statistics under uniaxial loads has been extensively investigated in Feng and Chen (2018, 2019), including consideration of non-Gaussian distribution character.

Accuracy of Approach for Time-Varying Mean Displacement

The time-varying mean displacement was also analyzed from the state-space equation, Eq. (15a), using the response variance and covariance being estimated from statistical linearization with n=2. The results are shown in Fig. 18 and compared with those estimated from simulation that are reported in Fig. 16. It is evident that the analytical estimations under both biaxial and uniaxial loads are very close to that by simulation.

Parametric Study

To further investigate the accuracy of the reduced-order building model and statistical linearization approach, and to examine the

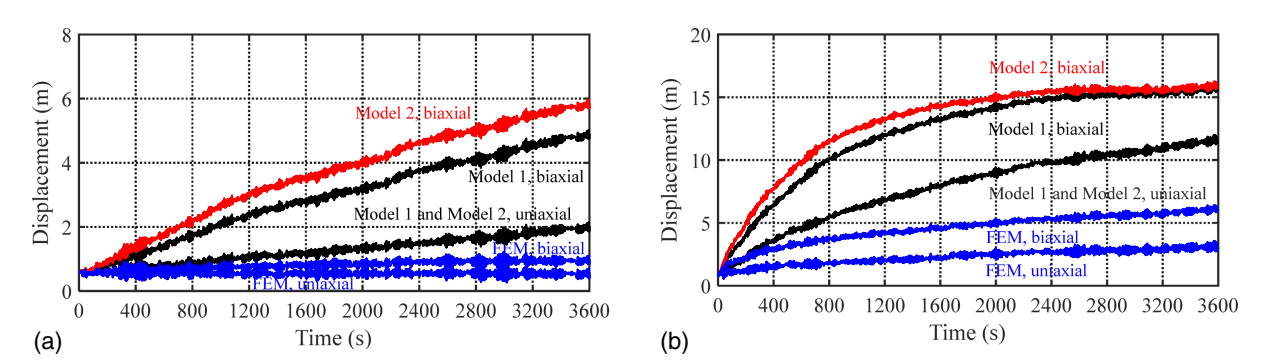


Fig. 16. Time-varying mean displacement at building top: (a) $U_H = 60$ m/s; and (b) $U_H = 80$ m/s.

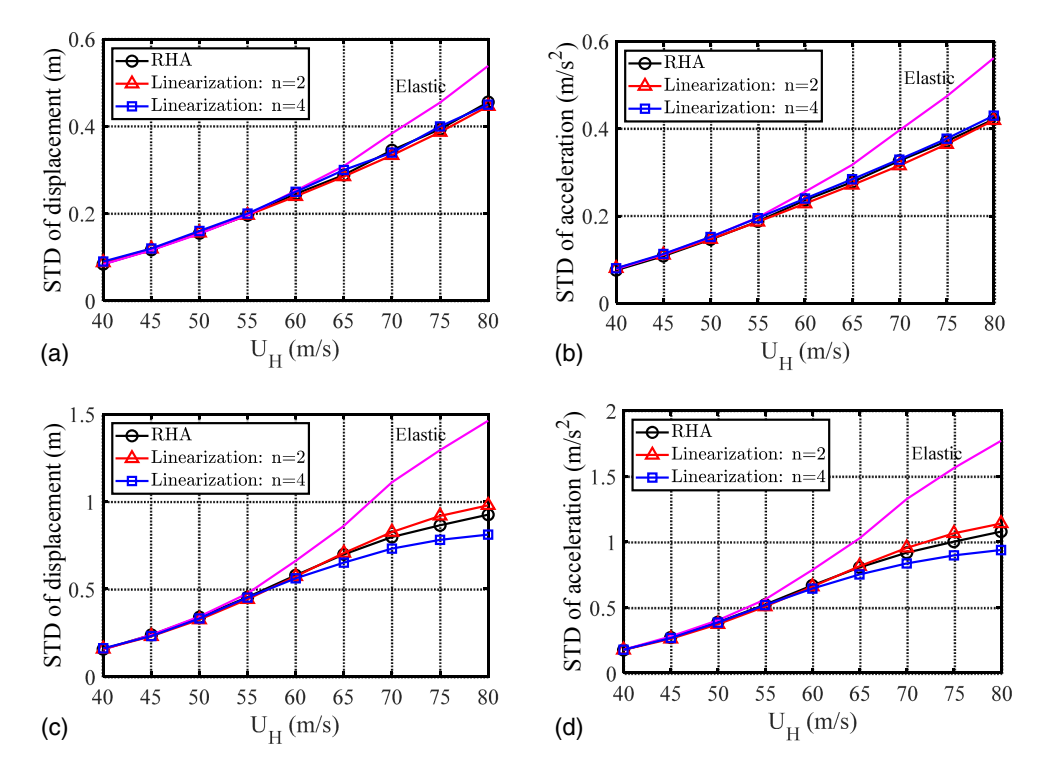


Fig. 17. Performance of statistical linearization approach in estimating STDs of responses: (a) alongwind displacement; (b) alongwind acceleration; (c) crosswind displacement; and (d) crosswind acceleration.

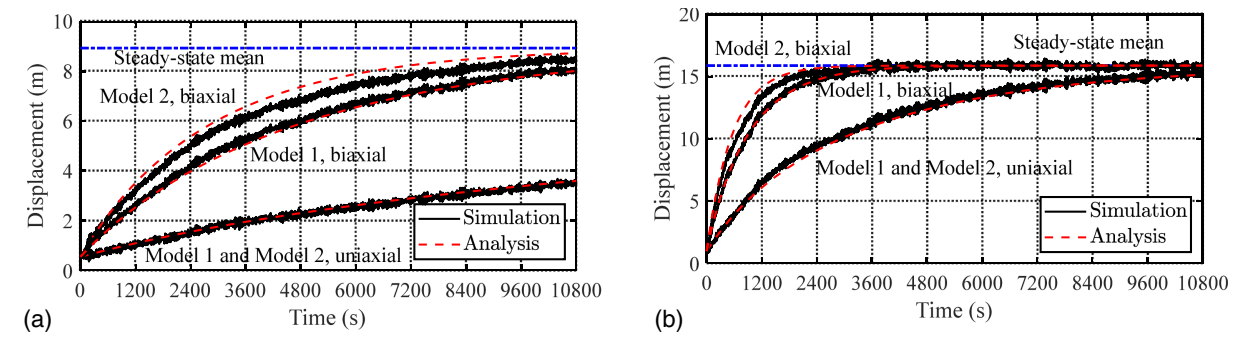


Fig. 18. Comparison of time-varying mean displacements at the building top: (a) $U_H = 60 \text{ m/s}$; and (b) $U_H = 80 \text{ m/s}$.

influence of biaxial interaction for a wide range of parameters, the alongwind load or crosswind load was modified by multiplying a loading factor and the corresponding building response is quantified. Fig. 19 shows the results where the alongwind load is scaled

up by a factor of 2.30. As a result, the alongwind displacement is close to the crosswind displacement in magnitude. As previously mentioned, there is a certain level of low-frequency component in the alongwind displacement at higher wind speeds due to the high

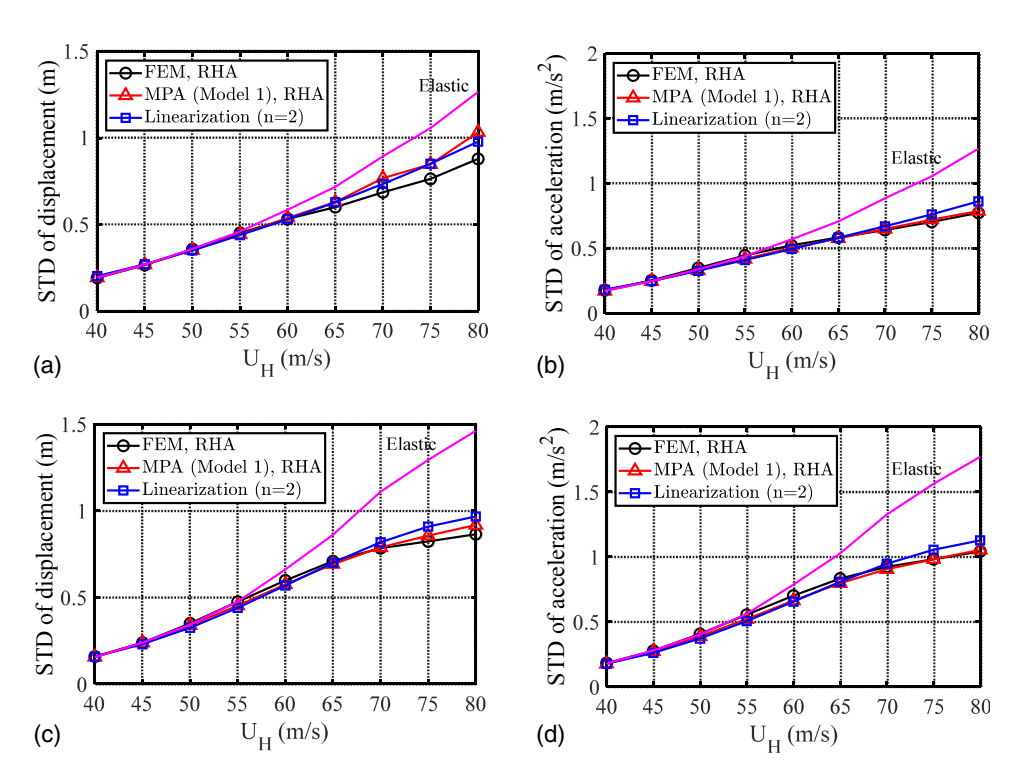


Fig. 19. STDs of building responses under different wind speeds where the alongwind load is scaled up by 2.30: (a) alongwind displacement; (b) alongwind acceleration; (c) crosswind displacement; and (d) crosswind acceleration.

level of yielding. On the other hand, such a low-frequency component does not exist in the alongwind acceleration and crosswind displacement and acceleration. Therefore, even with this scaled-up alongwind loading, the alongwind acceleration remains lower than crosswind acceleration. It is evident that the reduced-order building model can give accurate estimations of responses compared with the nonlinear FE model. The performance of the linearization approach was also quite acceptable, with slight overestimations of alongwind acceleration and crosswind displacement, as well as acceleration at very high level of yielding. The response under uniaxial loads was also predicted using these three approaches, and similar performance was observed. The ratios of STDs under biaxial loads to that under uniaxial loads is shown in Fig. 10. The biaxial interaction leads to reduction in both alongwind and crosswind responses. The influence of biaxial interaction declines when both alongwind and crosswind responses become closer in magnitudes. To further understand the unique character of the alongwind displacement under both uniaxial and biaxial loads, the displacement response was separated into low-frequency background and resonant components, and the respective variances were computed. It was found that the biaxial interaction leads to decrease in resonant alongwind displacement but increase in the background alongwind displacement when the yielding level is high.

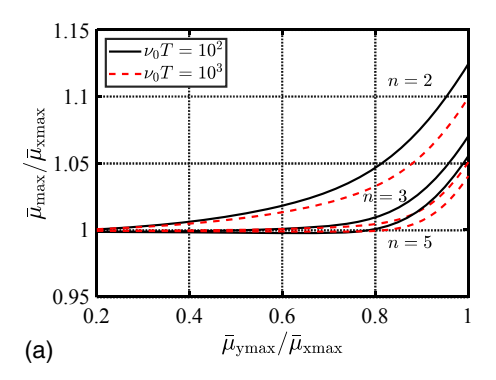
The cumulative distribution function (CDF) of the peak ductility demand μ_{max} , Eq. (10), contributed by both alongwind and crosswind responses, can be further discussed. It can be determined from the mean crossing rate $\nu(r)$ of the vector-valued process $\{q_x(t)/\Delta_x,q_y(t)/\Delta_y\}^T$ upcrossing the boundary $\mu_{\text{max}}=r$ (Rice 1944). In Appendix IV, the detailed formulations are presented for calculating the crossing rate when $q_x(t)$ and $q_y(t)$ are assumed to be Gaussian and independent stochastic processes. The mean of μ_{max} , $\bar{\mu}_{\text{max}}$, corresponds to nonexceeding probability of p=0.57. Chen and Huang (2009) and Gong and Chen (2014) presented a

comprehensive study for n = 2. In Gong and Chen (2014), the combination of non-Gaussian processes was also investigated.

 $\bar{\mu}_{\mathrm{max}}$ can be related to the means of two single peak ductility demands $\mu_{\text{xmax}} = \max_{\text{For all t}}[|q_x(t)|/\Delta_x]$ and $\mu_{\text{ymax}} = \max_{\text{For all t}}[|q_y(t)|/\Delta_x]$ Δ_y], i.e., $\bar{\mu}_{xmax}$ and $\bar{\mu}_{ymax}$. $\bar{\mu}_{xmax} = g_{|x|}\sigma_x/\Delta_x$ and $\bar{\mu}_{ymax} = g_{|y|}\sigma_y/\Delta_x$ Δ_y , where $g_{|x|}$ and $g_{|y|}$ are peak factors for $|q_x(t)|$ and $|q_y(t)|$. Without loss of generality, it is assumed $\bar{\mu}_{xmax} \ge \bar{\mu}_{ymax}$ and $\nu_{0x}T \approx \nu_{0y}T \approx \nu_0 T$. Denote ν_{0x} and ν_{0y} as the crossing rates at zero mean of the processes, as $\nu_{0x} \approx f_x = 0.173$ Hz, $\nu_{0y} \approx f_y =$ 0.164 Hz. For T = 600 s, we have $\nu_{0x}T \approx \nu_{0y}T \approx 10^2$, and thus $g_{|\mathbf{x}|} = g_{|\mathbf{y}|} = 3.43$ estimated by the Davenport formula. Fig. 20(a) displays the ratio $\bar{\mu}_{\rm max}/\bar{\mu}_{\rm xmax}$ against the ratio $\bar{\mu}_{\rm ymax}/\bar{\mu}_{\rm xmax}$ for $\nu_{0x}T = \nu_{0y}T = \nu_0T = 10^2$ and 10^3 with n = 2, 3 and 5 from upcrossing theory. It is observed that the ratio $\bar{\mu}_{\max}/\bar{\mu}_{\max}$ increases with increasing ratio $\bar{\mu}_{ymax}/\bar{\mu}_{xmax}$, and decreases with the increasing value of n. At $\bar{\mu}_{ymax}/\bar{\mu}_{xmax}=1$, the ratio $\bar{\mu}_{max}/\bar{\mu}_{xmax}$ is close to 1.12, 1.07, and 1.06 for n = 2, 3 and 5 when $\nu_0 T = 10^2$, representing 12%, 7% and 6% increase in the combined mean peak as compared to the single action. The contribution of smaller component is even less significant to the combined response (demand) when n is larger. Fig. 20(b) illustrates the peak ductility demand calculated from responses in the aforementioned parametric study using FE modeling and MPA with RHA. The simulation results match the theoretical prediction.

Conclusions

The inelastic response of tall buildings under simultaneous actions of both alongwind and crosswind loadings can be well represented by a reduced-order building model in terms of fundamental modes. The hysteretic relationships of generalized restoring forces and



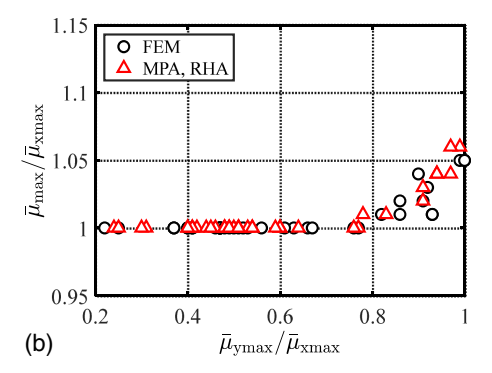


Fig. 20. Mean peak ductility demand of building top displacement: (a) theoretical results; and (b) simulation results.

displacements were determined by static modal pushover analysis using a high-fidelity nonlinear FE model with distributed plasticity, and then represented by a biaxial hysteresis model. This procedure leads to state-space equations of the building motion that can be solved by RHA or by the statistical linearization approach. Use of such a reduced-order building model can significantly improve computational efficiency, and thus is more suitable for parametric study and consideration of various uncertainties in structural reliability analysis. Through the response analysis of a 60-story building and a comprehensive parametric study, this study demonstrated the effectiveness of the analysis framework using the reduced building model.

The action of mean wind load leads to inelastic displacement drift until reaching the steady-state level, which is determined by the mean load and postyielding stiffness. The fluctuating displacement around the time-varying mean component can be estimated without consideration of the mean load because the hysteresis loop with nonzero mean load is simply to shift the average center position of the loop from the origin to a new position without the change of the shape. The numerical results illustrated that the reduced building model with RHA can lead to accurate estimations of fluctuating inelastic responses even with large ductility demand. The statistical linearization approach also provided quite accurate estimation of alongwind displacement, while some differences were observed in the inelastic crosswind response and alongwind acceleration when the ductility demand or yielding level was very high. The statistical linearization approach can be further improved by considering the non-Gaussian probability distribution of response caused by yielding. The alongwind displacement with high ductility demand features remarkable low-frequency background response, which was not observed in alongwind acceleration and crosswind displacement and acceleration. The alongwind displacement is more susceptible to the inherent issue of hysteretic model in terms of displacement drift, force relaxation, and nonclosure of hysteretic loops when subjected to short unloading-reloading paths. It poses a challenge to the estimations of low-frequency component when the yielding level is high, the power law parameter of hysteretic model and the postyielding stiffness ratio are low.

The biaxial interaction leads to reduction in one of fluctuating inelastic response with a lower magnitude due to additional hysteretic damping from increased level of yielding. The biaxial interaction has less influence on the fluctuating inelastic response with higher magnitude. The effect of biaxial interaction on the combined responses, such as peak ductility demand contributed by biaxial responses, is less significant. One exception can be expected when both alongwind and crosswind responses have larger ductility demands, where the biaxial interaction leads to increase in the low-frequency background component of alongwind displacement.

As a result, the alongwind displacement under biaxial loads can be increased. The effect of biaxial interaction will also be influenced by correlation coefficient of alongwind and crosswind responses.

With the reduced-order building model, the time-varying mean displacement can be computed from the solution of state-space equation. Numerical results showed that the prediction of time-varying mean was very sensitive to the modeling of transition from elastic to inelastic region and postyielding stiffness in the hysteretic relation between generalized restoring forces and displacements. The action of biaxial loads leads to faster growing time-varying mean displacement compared with the action of uniaxial loads. The steady-state mean responses under uniaxial and biaxial loadings are identical. Future research efforts are needed for consistent estimation of time-varying mean displacement as compared with that from FE models.

It should be noted that the framework presented in this study can also be used for buildings with 3D coupled mode shapes, where the relations of generalized forces and displacements in linear elastic range remain uncoupled. The correlation/coherence of alongwind and crosswind loadings can be further considered. The correlation of generalized displacements is normally lower than that of the generalized wind forces, and can only potentially affect the influence of biaxial interaction of the generalized restoring forces. It is expected that the biaxial interaction of the generalized restoring forces has a similar effect on coupled building response, while it should be explored in future study.

Appendix I. Coefficients for Time-Varying Mean Response

For the time-varying mean response, coefficients E_{xi} and E_{yi} (i = 1 - 4) are expressed as

$$E_{x1} = E[|\dot{q}_{x}||z_{x}|^{n-1}z_{x}]$$

$$= \frac{\sigma_{\dot{q}_{x}}\sigma_{z_{x}}^{n}}{\sqrt{2\pi}} \int_{-\infty}^{\infty} g_{x1}(r) \left| \left(r + \frac{\mu_{z_{x}}}{\sigma_{z_{x}}} \right) \right|^{n-1} \left(r + \frac{\mu_{z_{x}}}{\sigma_{z_{x}}} \right) \exp\left(-\frac{r^{2}}{2} \right) dr$$
(28)

$$E_{x2} = E[\dot{q}_x | z_x|^n] = \frac{\sigma_{\dot{q}_x} \sigma_{z_x}^n}{\sqrt{2\pi}} \int_{-\infty}^{\infty} g_{x2}(r) \left| \left(r + \frac{\mu_{z_x}}{\sigma_{z_x}} \right) \right|^n \exp\left(-\frac{r^2}{2} \right) dr$$
(29)

$$E_{x3} = E[z_x |\dot{q}_y| |z_y|^{n-1}]$$

$$= \frac{\sigma_{z_x} \sigma_{\dot{q}_y} \sigma_{z_y}^{n-1}}{\sqrt{2\pi}} \int_{-\infty}^{\infty} g_{x3}(r) \left| r + \frac{\mu_{z_y}}{\sigma_{z_y}} \right|^{n-1} \exp\left(-\frac{r^2}{2}\right) dr \quad (30)$$

$$\begin{split} E_{x4} &= E[z_x \dot{q}_y | z_y |^{n-1} \operatorname{sgn}(z_y)] \\ &= \frac{\sigma_{z_x} \sigma_{\dot{q}_y} \sigma_{z_y}^{n-1}}{\sqrt{2\pi}} \int_{-\infty}^{\infty} g_{x4}(r) \left| r + \frac{\mu_{z_y}}{\sigma_{z_y}} \right|^{n-1} \operatorname{sgn}\left(r + \frac{\mu_{z_y}}{\sigma_{z_y}}\right) \\ &\times \exp\left(-\frac{r^2}{2}\right) dr \end{split} \tag{31}$$

$$g_{x1}(r) = 2\phi(\hat{\mu}_x)\sqrt{1 - \rho_{\hat{q}_x z_x}^2} + g_{x2}(r)[1 - 2\Phi(-\hat{\mu}_x)]$$
 (32)

$$g_{x2}(r) = \rho_{\dot{q}_x z_x} r + \frac{\mu_{\dot{q}_x}}{\sigma_{\dot{q}_x}} \tag{33}$$

$$\begin{split} g_{x3}(r) &= 2\phi(\hat{\mu}_y) \bigg(\rho_{z_x z_y} r + \frac{\mu_{z_x}}{\sigma_{z_x}} \bigg) \sqrt{(1 - \rho_{\hat{q}_y z_y}^2)} \\ &+ g_{x4}(r) [1 - 2\Phi(-\hat{\mu}_y)] \end{split} \tag{34}$$

$$g_{x4}(r) = \left(\rho_{z_x z_y} r + \frac{\mu_{z_x}}{\sigma_{z_x}}\right) \left(\rho_{\dot{q}_y z_y} r + \frac{\mu_{\dot{q}_y}}{\sigma_{\dot{q}_y}}\right) + \left(\rho_{z_x \dot{q}_y} - \rho_{z_x z_y} \rho_{\dot{q}_y z_y}\right)$$
(35)

$$E_{y1} = E[z_{y}|\dot{q}_{x}||z_{x}|^{n-1}]$$

$$= \frac{\sigma_{z_{y}}\sigma_{\dot{q}_{x}}\sigma_{z_{x}}^{n-1}}{\sqrt{2\pi}} \int_{-\infty}^{\infty} g_{y1}(r) \left| r + \frac{\mu_{z_{x}}}{\sigma_{z_{x}}} \right|^{n-1} \exp\left(-\frac{r^{2}}{2}\right) dr \quad (36)$$

$$\begin{split} E_{y2} &= E[z_y \dot{q}_x | z_x |^{n-1} \mathrm{sgn}(z_x)] \\ &= \frac{\sigma_{z_y} \sigma_{\dot{q}_x} \sigma_{z_x}^{n-1}}{\sqrt{2\pi}} \int_{-\infty}^{\infty} g_{y2}(r) \left| r + \frac{\mu_{z_x}}{\sigma_{z_x}} \right|^{n-1} \mathrm{sgn}\left(r + \frac{\mu_{z_x}}{\sigma_{z_x}}\right) \\ &\times \exp\left(-\frac{r^2}{2}\right) dr \end{split} \tag{37}$$

$$E_{y3} = E[|\dot{q}_{y}||z_{y}|^{n-1}z_{y}]$$

$$= \frac{\sigma_{\dot{q}_{y}}\sigma_{z_{y}}^{n}}{\sqrt{2\pi}} \int_{-\infty}^{\infty} g_{y3}(r) \left| \left(r + \frac{\mu_{z_{y}}}{\sigma_{z_{y}}} \right) \right|^{n-1} \left(r + \frac{\mu_{z_{y}}}{\sigma_{z_{y}}} \right) \exp\left(-\frac{r^{2}}{2} \right) dr$$
(38)

$$E_{y4} = E[\dot{q}_{y}|z_{y}|^{n}] = \frac{\sigma_{\dot{q}_{y}}\sigma_{z_{y}}^{n}}{\sqrt{2\pi}} \int_{-\infty}^{\infty} g_{y4}(r) \left| \left(r + \frac{\mu_{z_{y}}}{\sigma_{z_{y}}} \right) \right|^{n} \exp\left(-\frac{r^{2}}{2} \right) dr$$
(39)

$$\begin{split} g_{y1}(r) &= 2 \phi(\hat{\mu}_x) \left(\rho_{z_x z_y} r + \frac{\mu_{z_y}}{\sigma_{z_y}} \right) \sqrt{(1 - \rho_{\hat{q}_x z_x}^2)} \\ &+ g_{y2}(r) [1 - 2 \Phi(-\hat{\mu}_x)] \end{split} \tag{40}$$

$$g_{y2}(r) = \left(\rho_{z_x z_y} r + \frac{\mu_{z_y}}{\sigma_{z_y}}\right) \left(\rho_{\dot{q}_x z_x} r + \frac{\mu_{\dot{q}_x}}{\sigma_{\dot{q}_x}}\right) + (\rho_{z_y \dot{q}_x} - \rho_{z_x z_y} \rho_{\dot{q}_x z_x})$$
(41)

$$g_{y3}(r) = 2\phi(\hat{\mu}_y)\sqrt{1 - \rho_{\hat{q}_y z_y}^2} + g_{y4}(r)[1 - 2\Phi(-\hat{\mu}_y)]$$
 (42)

$$g_{y4}(r) = \rho_{\dot{q}_y z_y} r + \frac{\mu_{\dot{q}_y}}{\sigma_{\dot{q}_y}}$$
 (43)

where $\phi(x)$ and $\Phi(x)$ = standard Gaussian PDF and CDF; and $\hat{\mu}_x(r) = (\rho_{\dot{q}_x z_x} r + \mu_{\dot{q}_x}/\sigma_{\dot{q}_x})/\sqrt{(1-\rho_{\dot{q}_x z_x}^2)}$ and $\hat{\mu}_y(r) = (\rho_{\dot{q}_y z_y} r + \mu_{\dot{q}_y}/\sigma_{\dot{q}_y})/\sqrt{(1-\rho_{\dot{q}_x z_y}^2)}$.

Appendix II. Linearization Coefficients with Zero Mean Excitation

Under the assumption that \dot{q}_x , \dot{q}_y , z_x , z_y follow joint Gaussian distribution, the linearization coefficients C_{xi} and C_{yi} (i = 1 - 4) are calculated as

$$C_{x1} = 1 - \beta_x F_{x1} - \gamma_x F_{x2} \tag{44}$$

$$C_{x2} = -\beta_y F_{x3} - \gamma_y F_{x4} \tag{45}$$

$$C_{x3} = -\beta_x F_{x5} - \gamma_x F_{x6} - \beta_y F_{x7} - \gamma_y F_{x8}$$
 (46)

$$C_{x4} = -\beta_{y} F_{x9} - \gamma_{y} F_{x10} \tag{47}$$

$$F_{x1} = E[z_x | z_x |^{n-1} \operatorname{sgn}(\dot{q}_x)] = \frac{\sigma_{z_x}^n}{\pi} 2^{\frac{n}{2}} \Gamma\left(\frac{n+2}{2}\right) I_{sx}$$
 (48)

$$F_{x2} = E[|z_x|^n] = \frac{\sigma_{z_x}^n}{\sqrt{\pi}} \Gamma\left(\frac{n+1}{2}\right) 2^{\frac{n}{2}}$$
 (49)

$$\begin{split} F_{x3} &= E[z_x | z_y |^{n-1} \mathrm{sgn}(\dot{q}_y)] \\ &= \frac{\sigma_{z_x} \sigma_{z_y}^{n-1}}{\pi} 2^{\frac{u}{2}} \Gamma \bigg(\frac{n+2}{2} \bigg) \\ &\times \left[\frac{2}{n} (1 - \rho_{\dot{q}_y z_y}^2)^{\frac{n-1}{2}} (\rho_{z_x \dot{q}_y} - \rho_{z_x z_y} \rho_{\dot{q}_y z_y}) + \rho_{z_x z_y} I_{sy} \right] \end{split} \tag{50}$$

$$F_{x4} = E[z_x z_y | z_y|^{n-2}] = \frac{\rho_{z_x z_y} \sigma_{z_x} \sigma_{z_y}^{n-1}}{\sqrt{\pi}} 2^{\frac{n}{2}} \Gamma\left(\frac{n+1}{2}\right)$$
 (51)

$$F_{x5} = nE[|\dot{q}_x||z_x|^{n-1}]$$

$$= \frac{n\sigma_{\dot{q}_x}\sigma_{z_x}^{n-1}}{\pi} 2^{\frac{n}{2}}\Gamma\left(\frac{n+2}{2}\right) \left[\frac{2}{n} (1 - \rho_{\dot{q}_x z_x}^2)^{\frac{n+1}{2}} + \rho_{\dot{q}_x z_x} I_{sx}\right]$$
(52)

$$F_{x6} = nE[\dot{q}_x z_x | z_x|^{n-2}] = \frac{n\rho_{\dot{q}_x z_x} \sigma_{\dot{q}_x} \sigma_{\dot{q}_x}^{n-1}}{\sqrt{\pi}} 2^{\frac{n}{2}} \Gamma\left(\frac{n+1}{2}\right)$$
 (53)

$$F_{x7} = E[|\dot{q}_{y}||z_{y}|^{n-1}]$$

$$= \frac{\sigma_{\dot{q}_{y}}\sigma_{z_{y}}^{n-1}}{\pi} 2^{\frac{n}{2}} \Gamma\left(\frac{n+2}{2}\right) \left[\frac{2}{n} (1 - \rho_{\dot{q}_{y}z_{y}}^{2})^{\frac{n+1}{2}} + \rho_{\dot{q}_{y}z_{y}} I_{sy}\right]$$
(54)

$$F_{x8} = E[\dot{q}_y z_y | z_y|^{n-2}] = \frac{\rho_{\dot{q}_y z_y} \sigma_{\dot{q}_y} \sigma_{z_y}^{n-1}}{\sqrt{\pi}} 2^{\frac{n}{2}} \Gamma\left(\frac{n+1}{2}\right)$$
 (55)

$$\begin{split} F_{x9} &= (n-1)E[z_x|\dot{q}_y||z_y|^{n-2}\mathrm{sgn}(z_y)] \\ &= \frac{(n-1)\sigma_{z_x}\sigma_{\dot{q}_y}\sigma_{z_y}^{n-2}}{\pi(1-\rho_{\dot{q}_yz_y}^2)}2^{\frac{n}{2}}\Gamma\bigg(\frac{n+2}{2}\bigg) \\ &\times \left\{ \begin{aligned} &(\rho_{z_x\dot{q}_y}-\rho_{z_xz_y}\rho_{\dot{q}_yz_y}) & \left[\frac{2(n-2)}{n(n-1)}\rho_{\dot{q}_yz_y}(1-\rho_{\dot{q}_yz_y}^2)^{\frac{n+1}{2}} \\ &+\frac{1}{n-1}(1-\rho_{\dot{q}_yz_y}^2)I_{sy}+\rho_{\dot{q}_yz_y}^2I_y \right] \\ &+(\rho_{z_xz_y}-\rho_{z_x\dot{q}_y}\rho_{\dot{q}_yz_y}) \left[\frac{2}{n}(1-\rho_{\dot{q}_yz_y}^2)^{\frac{n+1}{2}}+\rho_{\dot{q}_yz_y}I_{sy} \right] \end{aligned} \right\} \end{split} \end{split}$$

$$\begin{split} F_{x10} &= (n-1)E[z_x \dot{q}_y | z_y |^{n-2}] \\ &= \frac{(n-1)\sigma_{z_x}\sigma_{\dot{q}_y}\sigma_{z_y}^{n-2}}{\sqrt{\pi}(1-\rho_{\dot{q}_yz_y}^2)} \Gamma\bigg(\frac{n+1}{2}\bigg) 2^{\frac{n}{2}} \\ &\times \bigg\{ (\rho_{z_x \dot{q}_y} - \rho_{z_x z_y} \rho_{\dot{q}_y z_y}) \bigg[\frac{1}{n-1} (1-\rho_{\dot{q}_yz_y}^2) + \rho_{\dot{q}_yz_y}^2 \bigg] \\ &\quad + (\rho_{z_x z_y} - \rho_{z_x \dot{q}_y} \rho_{\dot{q}_y z_y}) \rho_{\dot{q}_y z_y} \bigg\} \end{split} \tag{57}$$

$$C_{v1} = -\beta_x F_{v3} - \gamma_x F_{v4} \tag{58}$$

$$C_{v2} = 1 - \beta_{v} F_{v1} - \gamma_{v} F_{v2} \tag{59}$$

$$C_{y3} = -\beta_x F_{y9} - \gamma_x F_{y10} \tag{60}$$

$$C_{v4} = -\beta_{v} F_{v5} - \gamma_{v} F_{v6} - \beta_{x} F_{v7} - \gamma_{x} F_{v8}$$
 (61)

$$F_{y1} = E[z_y|z_y|^{n-1}\operatorname{sgn}(\dot{q}_y)] = \frac{\sigma_{z_y}^n}{\pi} 2^{n/2} \Gamma\left(\frac{n+2}{2}\right) I_{sy}$$
 (62)

$$F_{y2} = E[|z_y|^n] = \frac{\sigma_{z_y}^n}{\sqrt{\pi}} \Gamma\left(\frac{n+1}{2}\right) 2^{\frac{n}{2}}$$
 (63)

$$\begin{split} F_{y3} &= E[z_{y}|z_{x}|^{n-1}\mathrm{sgn}(\dot{q}_{x})] \\ &= \frac{\sigma_{z_{y}}\sigma_{z_{x}}^{n-1}}{\pi}2^{\frac{n}{2}}\Gamma\bigg(\frac{n+2}{2}\bigg) \\ &\times \left[\frac{2}{n}(1-\rho_{\dot{q}_{x}z_{x}}^{2})^{\frac{n-1}{2}}(\rho_{z_{y}\dot{q}_{x}}-\rho_{z_{y}z_{x}}\rho_{\dot{q}_{x}z_{x}}) + \rho_{z_{y}z_{x}}I_{sx}\right] \quad (64) \end{split}$$

$$F_{y4} = E[z_y z_x | z_x |^{n-2}] = \frac{\rho_{z_y z_x} \sigma_{z_y} \sigma_{z_x}^{n-1}}{\sqrt{\pi}} 2^{\frac{n}{2}} \Gamma\left(\frac{n+1}{2}\right)$$
 (65)

$$F_{y5} = nE[|\dot{q}_{y}||z_{y}|^{n-1}]$$

$$= \frac{n\sigma_{\dot{q}_{y}}\sigma_{z_{y}}^{n-1}}{\pi}2^{\frac{n}{2}}\Gamma\left(\frac{n+2}{2}\right)\left[\frac{2}{n}(1-\rho_{\dot{q}_{y}z_{y}}^{2})^{\frac{n+1}{2}} + \rho_{\dot{q}_{y}z_{y}}I_{s}\right]$$
(66)

$$F_{y6} = nE[\dot{q}_{y}z_{y}|z_{y}|^{n-2}] = \frac{n\rho_{\dot{q}_{y}z_{y}}\sigma_{\dot{q}_{y}}\sigma_{z_{y}}^{n-1}}{\sqrt{\pi}}2^{\frac{n}{2}}\Gamma\left(\frac{n+1}{2}\right)$$
(67)

$$F_{y7} = E[|\dot{q}_x||z_x|^{n-1}]$$

$$= \frac{\sigma_{\dot{q}_x}\sigma_{z_x}^{n-1}}{\pi} 2^{\frac{n}{2}} \Gamma\left(\frac{n+2}{2}\right) \left[\frac{2}{n} (1 - \rho_{\ddot{q}_x z_x}^2)^{\frac{n+1}{2}} + \rho_{\dot{q}_x z_x} I_{sx}\right]$$
(68)

$$F_{y8} = E[\dot{q}_x z_x | z_x|^{n-2}] = \frac{\rho_{\dot{q}_x z_x} \sigma_{\dot{q}_x} \sigma_{z_x}^{n-1}}{\sqrt{\pi}} 2^{\frac{n}{2}} \Gamma\left(\frac{n+1}{2}\right)$$
 (69)

$$\begin{split} F_{y9} &= (n-1)E[z_{y}|\dot{q}_{x}||z_{x}|^{n-2}\mathrm{sgn}(z_{x})] \\ &= \frac{(n-1)\sigma_{z_{y}}\sigma_{\dot{q}_{x}}\sigma_{z_{x}}^{n-2}}{\pi(1-\rho_{\dot{q}_{x}z_{x}}^{2})}2^{\frac{n}{2}}\Gamma\left(\frac{n+2}{2}\right) \\ &\times \left\{ (\rho_{z_{y}\dot{q}_{x}}-\rho_{z_{y}z_{x}}\rho_{\dot{q}_{x}z_{x}}) \left[\frac{2(n-2)}{n(n-1)}\rho_{\dot{q}_{x}z_{x}}(1-\rho_{\dot{q}_{x}z_{x}}^{2})^{\frac{n+1}{2}} + \frac{1}{n-1}(1-\rho_{\dot{q}_{x}z_{x}}^{2})I_{sx} + \rho_{\dot{q}_{x}z_{x}}^{2}I_{sx} \right] \right\} \\ &+ (\rho_{z_{y}z_{x}}-\rho_{z_{y}\dot{q}_{x}}\rho_{\dot{q}_{x}z_{x}}) \left[\frac{2}{n}(1-\rho_{\dot{q}_{x}z_{x}}^{2})^{\frac{n+1}{2}} + \rho_{\dot{q}_{x}z_{x}}I_{sx} \right] \end{split}$$

$$\begin{split} F_{y10} &= (n-1)E[z_{y}\dot{q}_{x}|z_{x}|^{n-2}] \\ &= \frac{(n-1)\sigma_{z_{y}}\sigma_{\dot{q}_{x}}\sigma_{z_{x}}^{n-2}}{\sqrt{\pi}(1-\rho_{\dot{q}_{x}z_{x}}^{2})}\Gamma\left(\frac{n+1}{2}\right)2^{\frac{n}{2}} \\ &\times \left\{ (\rho_{z_{y}\dot{q}_{x}} - \rho_{z_{y}z_{x}}\rho_{\dot{q}_{x}z_{x}})\left[\frac{1}{n-1}(1-\rho_{\dot{q}_{x}z_{x}}^{2}) + \rho_{\dot{q}_{x}z_{x}}^{2}\right] \right. \\ &\left. + (\rho_{z_{y}z_{x}} - \rho_{z_{y}\dot{q}_{x}}\rho_{\dot{q}_{x}z_{x}})\rho_{\dot{q}_{x}z_{x}}\right\} \end{split} \tag{71}$$

where $I_{sx} = 2 \int_{l_x}^{\pi/2} \sin^n \theta d\theta$; $l_x = \tan^{-1}[(1 - \rho_{\dot{q}_x z_x}^2)^{0.5}/\rho_{\dot{q}_x z_x}]$; $I_{sy} = 2 \int_{l_y}^{\pi/2} \sin^n \theta d\theta$; and $l_y = \tan^{-1}[(1 - \rho_{\dot{q}_y z_y}^2)^{0.5}/\rho_{\dot{q}_y z_y}]$.

Appendix III. Prove of Steady-State Mean Displacement

By assuming z_x , z_y , \dot{q}_x , \dot{q}_y follow joint Gaussian distribution, E_{xi} and E_{yi} (i=1-4) are given in Appendix I.

As $\beta_x = \gamma_x$, $\beta_y = \gamma_y$ and $\dot{\mu}_v = 0$, Eq. (15) can be simplified as

$$\beta_x(E_{x1} + E_{x2}) + \beta_v(E_{x3} + E_{x4}) = 0 \tag{72}$$

$$\beta_x(E_{v1} + E_{v2}) + \beta_v(E_{v3} + E_{v4}) = 0 \tag{73}$$

Feng and Chen (2018) have proved $\mu_{z_x}=0$ by using the monotonous property of the integrand in $E_{x1}+E_{x2}=0$. As both integrand in E_{x3} and E_{x4} are odd, $E_{x3}=0$ and $E_{x4}=0$ can be further obtained. As Eqs. (72) and (73) have unique solution and all the integrands in E_{y1} to E_{y4} are odd when $\mu_{z_x}=0$ and $\mu_{z_y}=0$. Also, $E_{y1}=0$, $E_{y2}=0$, $E_{y3}=0$ and $E_{y4}=0$ can be validated when $\mu_{z_x}=0$ and $\mu_{z_y}=0$. Above all, by solving Eqs. (72) and (73) simultaneously, the unique solution is $\mu_{z_x}=0$ and $\mu_{z_y}=0$.

Appendix IV. Extreme Value Distribution of Combined Responses

The CDF of the peak ductility demand $\mu_{\max} = \max_{\text{For all t}} [|q_x(t)/\Delta_x|^n + |q_y(t)/\Delta_y|^n]^{\frac{1}{n}} = \max_{\text{For all t}} [|\mu_x(t)|^n + |\mu_y(t)|^n]^{\frac{1}{n}}$ where $\mu_x = q_x/\Delta_x$ and $\mu_y = q_y/\Delta_y$ with $0 \le t \le T$ can be expressed as

$$F_{\mu_{\text{max}}}(r) = \exp[-\nu(r)T] \tag{74}$$

where $\nu(r)$ = mean upcrossing rate of the vector-valued process $\{\mu_x(t), \mu_y(t)\}^T$ at the boundary $r = [|\mu_x(t)|^n + |\mu_y(t)|^n]^{\frac{1}{n}}$ (Rice 1944), as follows:

$$\nu(r) = \oint E[\dot{r}_n^+|\{x,y\}] f_{xy}(,y) ds \tag{75}$$

where $f_{xy}(x, y) = \text{joint PDF of } \mu_x(t) \text{ and } \mu_y(t)$.

$$E[\dot{r}_n^+|\{x,y\}] = \int_0^\infty w f_{\dot{r}_n^+|\{x,y\}}(w) dw$$
 (76)

where $f_{\dot{r}_n^+|\{x,y\}}(w) = \text{PDF of } \dot{r}_n^+|\{x,y\} \text{ defined as}$

$$\dot{r}_{n}^{+}|\{x,y\} = (|x|^{n} + |y|^{n})^{\frac{1}{n}-1}[|x|^{n-1}\operatorname{sgn}(x)\dot{\mu}_{x} + |y|^{n-1}\operatorname{sgn}(y)\dot{\mu}_{y}]|\{x,y\}$$

$$(77)$$

When $\mu_x(t)$ and $\mu_y(t)$ are jointly Gaussian and independent, $\mu_x(t)$, $\mu_y(t)$, $\dot{\mu}_x(t)$, and $\dot{\mu}_y(t)$ are Gaussian and mutually independent, as follows:

$$E[\dot{r}_n^+|\{x,y\}] = \frac{\sigma_{\dot{r}_n^+}}{\sqrt{2\pi}}$$
 (78)

$$\nu(r) = \int_0^{2\pi} \frac{\sigma_{r_n^+}}{\sqrt{2\pi}} f_{xy}(x, y) r_0 d\theta$$
 (79)

where

$$\sigma_{\dot{r}_n^+} = 2\pi (|x|^n + |y|^n)^{\frac{1}{n}} [x^{2(n-1)} \nu_{0x}^2 \sigma_x^2 + y^{2(n-1)} \nu_{0y}^2 \sigma_y^2]^{\frac{1}{2}}$$
 (80)

$$f_{xy}(x,y) = \frac{1}{2\pi\sigma_x\sigma_y} \exp\left[-\frac{1}{2} \left(\frac{r_0^2 \cos^2 \theta}{\sigma_x^2} + \frac{r_0^2 \sin^2 \theta}{\sigma_y^2}\right)\right]$$
(81)

$$r_0 = r(|\cos \theta|^n + |\sin \theta|^n)^{-\frac{1}{n}}$$
 (82)

$$x = r_0 \cos \theta; \qquad y = r_0 \sin \theta \tag{83}$$

$$\nu_{0x} = \sigma_{\dot{x}}/(2\pi\sigma_x); \qquad \nu_{0y} = \sigma_{\dot{y}}/(2\pi\sigma_y) \tag{84}$$

Data Availability Statement

Some or all data, models, or code that support the findings of this study are available from the corresponding author upon reasonable request.

Acknowledgments

The support for this work provided in part by NSF Grant No. CMMI-1536108 is greatly acknowledged.

References

- AIJ (Architectural Institute of Japan). 2004. AIJ recommendations for load on buildings. Tokyo: AIJ.
- ASCE. 2019. Prestandard for performance-based wind design. Reston, VA: ASCE.
- Beck, A. T., I. A. Kougioumtzoglou, and K. R. dos Santos. 2014. "Optimal performance-based design of non-linear stochastic dynamical RC structures subject to stationary wind excitation." *Eng. Struct.* 78 (Nov): 145–153. https://doi.org/10.1016/j.engstruct.2014.07.047.

- Bouc, R. 1967. "Forced vibrations of mechanical systems with hysteresis." In *Proc.*, *4th Conf. on Nonlinear Oscillations*. Wuhan, China: Scientific Research Publishing.
- Charalampakis, A. E., and V. K. Koumousis. 2009. "A Bouc-Wen model compatible with plasticity postulates." *J. Sound Vib.* 322 (4–5): 954–968. https://doi.org/10.1016/j.jsv.2008.11.017.
- Chen, X., and G. Huang. 2009. "Evaluation of peak resultant response for wind-excited tall buildings." Eng. Struct. 31 (4): 858–868.
- Chen, X., and A. Kareem. 2005a. "Coupled dynamic analysis and equivalent static wind loads on buildings with 3-D modes." *J. Struct. Eng.* 131 (7): 1071–1082. https://doi.org/10.1061/(ASCE)0733-9445(2005) 131:7(1071).
- Chen, X., and A. Kareem. 2005b. "Dynamic wind effects on buildings with 3-D coupled modes: Application of high frequency force balance measurements." *J. Eng. Mech.* 131 (11): 1115–1125. https://doi.org/10.1061/(ASCE)0733-9399(2005)131:11(1115).
- Chen, X., and A. Kareem. 2005c. "Proper orthogonal decomposition-based modeling, analysis, and simulation of dynamic wind load effects on structures." *J. Eng. Mech.* 131 (4): 325–339. https://doi.org/10.1061/(ASCE)0733-9399(2005)131:4(325).
- Chopra, A. K., and R. K. Goel. 2002. "A modal pushover analysis procedure for estimating seismic demands for buildings." *Earthquake Eng. Struct. Dyn.* 31 (3): 561–582. https://doi.org/10.1002/eqe.144.
- Chopra, A. K., and R. K. Goel. 2004. "A modal pushover analysis procedure to estimate seismic demands for unsymmetric-plan buildings." *Earthquake Eng. Struct. Dyn.* 33 (8): 903–927. https://doi.org/10.1002/eqe.380.
- Chopra, A. K., R. K. Goel, and C. Chintanapakdee. 2004. "Evaluation of a modified MPA procedure assuming higher modes as elastic to estimate seismic demands." *Earthquake Spectra* 20 (3): 757–778. https://doi.org /10.1193/1.1775237.
- Chuang, W. C., and S. M. Spence. 2017. "A performance-based design framework for the integrated collapse and non-collapse assessment of wind excited buildings." *Eng. Struct.* 150 (Nov): 746–758. https://doi .org/10.1016/j.engstruct.2017.07.030.
- Chuang, W. C., and S. M. Spence. 2019. "An efficient framework for the inelastic performance assessment of structural systems subject to stochastic wind loads." *Eng. Struct.* 179 (Jan): 92–105. https://doi.org/10 .1016/j.engstruct.2018.10.039.
- Davenport, A. G. 1964. "Note on the distribution of the largest value of a random function with application to gust loading." *Proc. Inst. Civ. Eng.* 28 (2): 187–196
- Ding, J., and X. Chen. 2015. "Fatigue damage evaluation of broad-band Gaussian and non-Gaussian wind load effects by a spectral method." *Probab. Eng. Mech.* 41 (Jul): 139–154.
- Feng, C., and X. Chen. 2018. "Inelastic responses of wind-excited tall buildings: Improved estimation and understanding by statistical linearization approaches." *Eng. Struct.* 159 (Mar): 141–154. https://doi.org/10 .1016/j.engstruct.2017.12.041.
- Feng, C., and X. Chen. 2019. "Estimation of inelastic crosswind response of base-isolated tall buildings: Performance of statistical linearization approaches." J. Struct. Eng. 145 (12): 04019161. https://doi.org/10 .1061/(ASCE)ST.1943-541X.0002465.
- Gani, F., and F. Légeron. 2012. "Relationship between specified ductility and strength demand reduction for single degree-of-freedom systems under extreme wind events." *J. Wind Eng. Ind. Aerodyn.* 109 (Oct): 31–45. https://doi.org/10.1016/j.jweia.2012.06.006.
- Ghaffary, A., and M. A. Moustafa. 2021. "Performance-based assessment and structural response of 20-story sac building under wind hazards through collapse." *J. Struct. Eng.* 147 (3): 04020346. https://doi.org/10.1061/(ASCE)ST.1943-541X.0002911.
- Goel, R. K., and A. K. Chopra. 2005. "Extension of modal pushover analysis to compute member forces." *Earthquake Spectra* 21 (1): 125–139. https://doi.org/10.1193/1.1851545.
- Gong, K., and X. Chen. 2014. "Estimation of extremes of combined two Gaussian and non-Gaussian response processes." *Int. J. Struct. Stab. Dyn.* 14 (3): 1350076. https://doi.org/10.1142/S0219455413500764.
- Griffis, L., V. Patel, S. Muthukumar, and S. Baldava. 2013. "A framework for performance-based wind engineering." In *Proc.*, *Advances in Hurricane Engineering*, 1205–1216. Reston, VA: ASCE.

- Hart, G. C., and A. Jain. 2014. "Performance-based wind evaluation and strengthening of existing tall concrete buildings in the Los Angeles region: Dampers, nonlinear time history analysis and structural reliability." Struct. Des. Tall Spec. Build. 23 (16): 1256–1274. https://doi.org /10.1002/tal.1139.
- Harvey, P. S., Jr., and H. P. Gavin. 2014. "Truly isotropic biaxial hysteresis with arbitrary knee sharpness." *Earthquake Eng. Struct. Dyn.* 43 (13): 2051–2057. https://doi.org/10.1002/eqe.2436.
- Hong, H. P. 2004. "Accumulation of wind induced damage on bilinear SDOF systems." Wind Struct. 7 (3): 145–158. https://doi.org/10.12989 /was.2004.7.3.145.
- Huang, J., and X. Chen. 2022. "Inelastic performance of high-rise buildings to simultaneous actions of alongwind and crosswind loads." *J. Struct. Eng.* 148 (2): 04021258. https://doi.org/10.1061/(ASCE)ST.1943-541X.0003236.
- Irwin, P. A. 2009. "Wind engineering research needs, building codes and project specific studies." In *Proc.*, 11th Americas Conf. on Wind Engineering. Ames, IA: American Association of Wind Engineering.
- Judd, J. P., and F. A. Charney. 2015. "Inelastic behavior and collapse risk for buildings subjected to wind loads." In *Proc.*, *Structures Congress*, 2483–2496. Reston, VA: ASCE.
- Judd, J. P., and F. A. Charney. 2016. "Wind performance assessment of buildings." In *Proc.*, Geotechnical and Structural Engineering Congress, 1259–1268. Reston, VA: ASCE.
- Kalkan, E., and S. K. Kunnath. 2007. "Assessment of current nonlinear static procedures for seismic evaluation of buildings." *Eng. Struct*. 29 (3): 305–316. https://doi.org/10.1016/j.engstruct.2006.04.012.
- Lee, C. S., and H. P. Hong. 2010. "Statistics of inelastic responses of hysteretic systems under bidirectional seismic excitations." *Eng. Struct*. 32 (8): 2074–2086. https://doi.org/10.1016/j.engstruct.2010.03.008.
- McKenna, F., M. H. Scott, and G. L. Fenves. 2010. "Nonlinear finite-element analysis software architecture using object composition." J. Comput. Civ. Eng. 24 (1): 95–107. https://doi.org/10.1061/(ASCE) CP.1943-5487.0000002.
- Mohammadi, A., A. Azizinamini, L. Griffis, and P. Irwin. 2019. "Performance assessment of an existing 47-story high-rise building under extreme wind loads." J. Struct. Eng. 145 (1): 04018232. https://doi.org/10.1061/(ASCE)ST.1943-541X.0002239.
- Mooneghi, M. A., P. Irwin, and A. G. Chowdhury. 2015. "Exploratory studies on a bilinear aeroelastic model for tall buildings." In *Proc.*, 14th Int. Conf. Wind Engineering. Paris: World Academy of Science, Engineering and Technology.
- NIST. 2017. Guidelines for nonlinear structural analysis for design of buildings. Gaithersburg, MD: NIST.
- Ohkuma, T., T. Kurita, and M. Ninomiya. 1997. "Response estimation based on energy balance for elasto-plastic vibration of tall building

- in across-wind direction." In *Proc., 7th Int. Conf. on Structural Safety and Reliability*, 1379–1386. Rotterdam, Netherlands: A.A. Balkema.
- Ouyang, Z., and S. M. Spence. 2021. "Performance-based wind-induced structural and envelope damage assessment of engineered buildings through nonlinear dynamic analysis." *J. Wind Eng. Ind. Aerodyn.* 208 (Jan): 104452. https://doi.org/10.1016/j.jweia.2020.104452.
- Park, S., and D. Yeo. 2018. "Second-order effects on wind-induced structural behavior of high-rise steel buildings." *J. Struct. Eng.* 144 (2): 04017209. https://doi.org/10.1061/(ASCE)ST.1943-541X.0001943.
- Park, Y. J., Y. K. Wen, and A. H. Ang. 1986. "Random vibration of hysteretic systems under bi-directional ground motions." *Earthquake Eng. Struct. Dyn.* 14 (4): 543–557.
- Rice, S. O. 1944. "Mathematical analysis of random noise." *Bell Labs Tech. J.* 23 (3): 282–332. https://doi.org/10.1002/j.1538-7305.1944.tb00874.x.
- Roberts, J. B., and P. D. Spanos. 2003. *Random vibration and statistical linearization*. Chelmsford, MA: Courier Corporation.
- Shinozuka, M., and C. M. Jan. 1972. "Digital simulation of random processes and its applications." J. Sound Vib. 25 (1): 111–128. https://doi.org/10.1016/0022-460X(72)90600-1.
- Tabbuso, P., S. M. Spence, L. Palizzolo, A. Pirrotta, and A. Kareem. 2016. "An efficient framework for the elasto-plastic reliability assessment of uncertain wind excited systems." *Struct. Saf.* 58 (Jan): 69–78. https://doi.org/10.1016/j.strusafe.2015.09.001.
- Tamura, Y., H. Yasui, and H. Marukawa. 2001. "Non-elastic responses of tall steel buildings subjected to across-wind forces." *Wind Struct.* 4 (2): 147–162. https://doi.org/10.12989/was.2001.4.2.147.
- Thyagarajan, R. S. 1989. "Modeling and analysis of hysteretic structural behavior." Ph.D. thesis, Earthquake Engineering Research Laboratory, California Institute of Technology.
- Tsujita, O., Y. Hayabe, and T. Ohkuma. 1997. "A study on wind-induced response for inelastic structure." In *Proc.*, 7th Int. Conf. on Structural Safety and Reliability, 1359–1366. Rotterdam, Netherlands: A.A. Balkema.
- Wang, C. H., and Y. K. Wen. 2000. "Evaluation of pre-Northridge low-rise steel buildings. I: Modeling." *J. Struct. Eng.* 126 (10): 1160–1168. https://doi.org/10.1061/(ASCE)0733-9445(2000)126:10(1160).
- Wen, Y. K. 1976. "Method for random vibration of hysteretic systems." J. Eng. Mech. Div. 102 (2): 249–263. https://doi.org/10.1061/JMCEA3 .0002106.
- Wong, C. W., Y. Q. Ni, and J. M. Ko. 1994. "Steady-state oscillation of hysteretic differential model. II: Performance analysis." *J. Eng. Mech.* 120 (11): 2299–2325. https://doi.org/10.1061/(ASCE)0733-9399(1994)120:11(2299).